Article

SOURCE DATA | TRANSPARENT PROCESS | OPEN ACCESS

THE EMBO JOURNAL

The glycine arginine-rich domain of the RNA-binding protein nucleolin regulates its subcellular localization

Ella Doron-Mandel[1,†,‡], Indrek Koppel[1,†,§], Ofri Abraham[1], Ida Rishal[1], Terika P Smith[2], Courtney N Buchanan[2], Pabitra K Sahoo[2], Jan Kadlec[3], Juan A Oses-Prieto[4], Riki Kawaguchi[5], Stefanie Alber[1], Eitan Erez Zahavi[1], Pierluigi Di Matteo[1], Agostina Di Pizio[1], Didi-Andreas Song[1], Nataliya Okladnikov[1], Dalia Gordon[1], Shifra Ben-Dor[6], Rebecca Haffner-Krausz[7], Giovanni Coppola[5], Alma L Burlingame[4], Pavel Jungwirth[3], Jeffery L Twiss[2] & Mike Fainzilber[1,*]

Abstract

Nucleolin is a multifunctional RNA Binding Protein (RBP) with diverse subcellular localizations, including the nucleolus in all eukaryotic cells, the plasma membrane in tumor cells, and the axon in neurons. Here we show that the glycine arginine rich (GAR) domain of nucleolin drives subcellular localization via protein-protein interactions with a kinesin light chain. In addition, GAR sequences mediate plasma membrane interactions of nucleolin. Both these modalities are in addition to the already reported involvement of the GAR domain in liquid-liquid phase separation in the nucleolus. Nucleolin transport to axons requires the GAR domain, and heterozygous GAR deletion mice reveal reduced axonal localization of nucleolin cargo mRNAs and enhanced sensory neuron growth. Thus, the GAR domain governs axonal transport of a growth controlling RNA-RBP complex in neurons, and is a versatile localization determinant for different subcellular compartments. Localization determination by GAR domains may explain why GAR mutants in diverse RBPs are associated with neurodegenerative disease.

Keywords subcellular localization; axonal transport; cell size regulation; local translation; protein–membrane interaction

Subject Categories Neuroscience; RNA Biology

DOI 10.15252/embj.2020107158 | Received 27 October 2020 | Revised 29 July 2021 | Accepted 3 August 2021 | Published online 13 September 2021

The EMBO Journal (2021) 40: e107158

Introduction

Nucleolin is a multifunctional, highly conserved, abundant RNA-binding protein (RBP) that is found in multiple subcellular compartments, including a relatively stable major nucleolar pool, and more dynamic nucleoplasmic, cytoplasmic, and plasma membrane complexes (Berger *et al*, 2015). The protein has been implicated in many cellular processes, including ribosome biogenesis, division and survival of cycling cells, oncogenesis and tumor growth, and size and length sensing in neurons and other large cells (Ugrinova *et al*, 2018; Rishal & Fainzilber, 2019). Although nucleolin is essential for cell viability (Ugrinova *et al*, 2007; Storck *et al*, 2009), and its cell surface localization in tumor cells has been exploited in the development of anti-cancer therapies (Berger *et al*, 2015; Gilles *et al*, 2016; Romano *et al*, 2019), the mechanisms underlying subcellular localization of nucleolin are still unclear.

Nucleolin is composed of a number of functional domains, including an amino-terminal charged region, a central region comprising four RNA-binding domains, and a carboxy-terminal glycine/arginine-rich (GAR) domain (Fig 1A). Early studies demonstrated that both RNA-binding and GAR domains are required for nucleolar localization of nucleolin (Creancier *et al*, 1993; Schmidt-Zachmann & Nigg, 1993; Pellar & DiMario, 2003), but the domain(s) involved in cytoplasmic, plasma membrane, or neuronal process localization of nucleolin have not been determined. We recently found that nucleolin is required for axonal trafficking of mRNAs that regulate neuronal growth or survival (Perry *et al*, 2016; Terenzio *et al*, 2018), and proposed that this RBP is

1 Departments of Biomolecular Sciences and Molecular Neuroscience, Weizmann Institute of Science, Rehovot, Israel
2 Department of Biological Sciences, University of South Carolina, Columbia, SC, USA
3 Institute of Organic Chemistry and Biochemistry, Czech Academy of Sciences, Prague, Czech Republic
4 Department of Pharmaceutical Chemistry, University of California San Francisco, San Francisco, CA, USA
5 Departments of Psychiatry and Neurology, Semel Institute for Neuroscience and Human Behavior, University of California Los Angeles, Los Angeles, CA, USA
6 Bioinformatics Unit, Life Sciences Core Facilities, Weizmann Institute of Science, Rehovot, Israel
7 Department of Veterinary Resources, Weizmann Institute of Science, Rehovot, Israel
*Corresponding author. Tel: +972 8 934 4266; E-mail: mike.fainzilber@weizmann.ac.il
†These authors contributed equally to this work
‡Present address: Department of Biological Sciences, Columbia University, New York, NY, USA
§Present address: Department of Chemistry and Biotechnology, Tallinn University of Technology, Tallinn, Estonia

a key component in a cell size sensing mechanism based on transport of mRNA from cell center to periphery, and retrograde transport of locally synthesized proteins encoded by these mRNAs (Rishal *et al*, 2012; Rishal & Fainzilber, 2019). These findings stimulated efforts to understand how nucleolin is trafficked to and retained in different subcellular compartments.

We recently demonstrated axonal transport of nucleolin in association with the molecular motor kinesin 1 (Kif5a) (Perry *et al*, 2016). We further showed that AS1411, a G-quadruplex forming nucleolin-targeted DNA aptamer (Bates *et al*, 2017), perturbs the association of nucleolin with the Kif5a motor complex (Perry *et al*, 2016), suggesting that the aptamer-binding domain of nucleolin should also mediate its axonal transport. Interestingly, previous studies had shown that the RBPs FMRP and FUS interact with G-quadruplex nucleic acid structures through GAR domains (Darnell *et al*, 2001; Ramos *et al*, 2003; Vasilyev *et al*, 2015; Yagi *et al*,

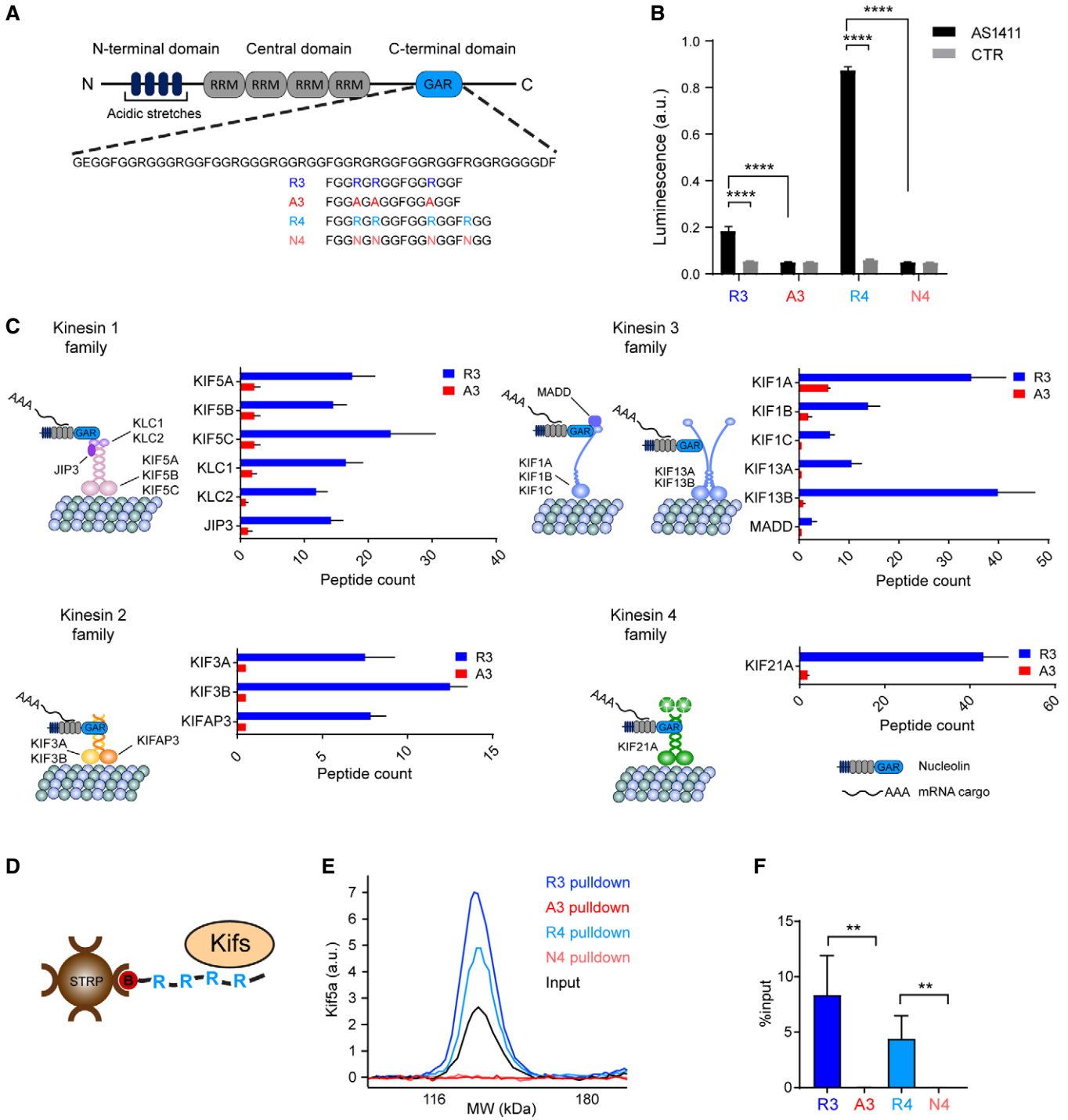

Figure 1.

Figure 1. The nucleolin GAR domain binds DNA aptamer AS1411 and kinesins.

A Domain structure of nucleolin. RRM—RNA recognition motif; GAR—glycine–arginine-rich domain. Amino acid sequence of the GAR domain is shown below. R3 and R4: peptides derived from the GAR domain C-terminus, efficiently binding AS1411 (see panel B). A3 designates the R3 peptide with three arginines substituted with alanines, and N4 designates the R4 peptide with four arginines substituted with asparagines.

B R3 and R4, but not the A3 and N4 peptides efficiently bind AS1411 in an ELISA assay with biotinylated peptides shown in (A) immobilized to streptavidin-coated plates. $n = 4$ technical replicates; means ± SEM; ****$P < 0.0001$ in AS1411 versus control aptamer, 2-way ANOVA with Sidak's post-test. a.u.—arbitrary units.

C Kinesin protein family members affinity purified by biotinylated R3 peptide from mouse sciatic nerve axoplasm, identified by mass spectrometry (schematics are based on (Hirokawa *et al*, 2009). Biotinylated A3 peptide served as a control. Mean spectral counts (normalized plus pseudocounts) ± SEM, $n = 3$ independent biological repeats. All proteins shown were found to significantly purify with R3, but not A3, with probability > 0.95 and a mean fold change > 2 by SAINTexpress analysis (http://crapome.org/).

D Schematic of kinesin pulldown from mouse sciatic nerve axoplasm, using biotinylated GAR peptides bound to streptavidin beads (STRP).

E Automated capillary electrophoresis immunoassay traces of Kif5a pulled down by biotinylated R3 and R4 peptides. Biotinylated A3 and N4 peptides, respectively, served as controls. 4.5% of input used for pulldowns was loaded alongside the pulldown samples. a.u.—arbitrary units.

F Quantification of (E). $n = 3$ independent biological repeats; means ± SEM; **$P < 0.01$, paired Student's t-test.

See also Fig EV1 and Appendix Fig S1.

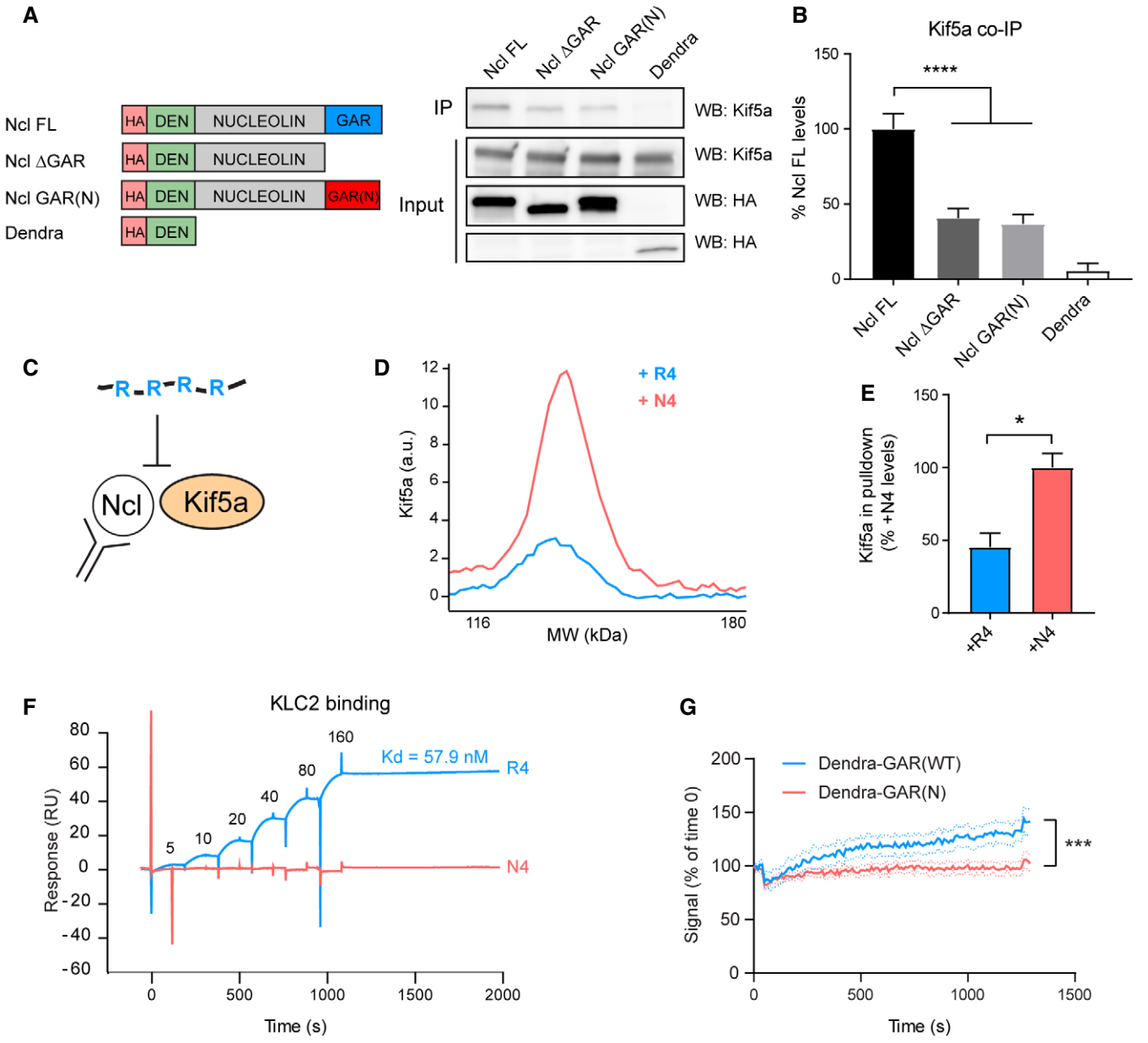

Figure 2.

Figure 2. Nucleolin–kinesin interaction is directly mediated by the GAR domain.

A GAR domain deletion or mutation perturbs binding to Kif5a. Co-immunoprecipitation analysis of Kif5a and HA-Dendra2-tagged nucleolin (both overexpressed in HEK-293 cells). IP was performed with HA antibody and probed in Western blot with anti-Kif5a and anti-HA antibodies. Ncl FL—HA-Dendra2-full-length nucleolin; Ncl ΔGAR—HA-Dendra2-nucleolin with a GAR domain deletion; Ncl GAR(N)—HA-Dendra2-nucleolin with all 10 arginines in the GAR domain mutated to asparagines; DEN—Dendra2. Note that HA input blots for HA-Dendra2 (Dendra) and the other three constructs are from the same membrane, but shown discontinuously owing to the different migration of these proteins in PAGE.

B Quantification of (A). $n = 3$ independent biological repeats; means ± SEM; $^{****}P < 0.0001$, ANOVA with Tukey's post-test.

C–E R4, but not N4 peptide, reduces Kif5a co-immunoprecipitation with nucleolin from mouse sciatic nerve axoplasm, assayed by automated capillary electrophoresis immunoassay for Kif5a. Schematic of the assay is shown in (C). Representative traces of the Kif5a immunoreactive peaks are shown in (D), and quantifications are shown in (E). Immunoprecipitated Kif5a levels are normalized with input levels and expressed relative to N4. $n = 3$ independent biological repeats; means ± SEM; $^{*}P < 0.05$, paired Student's t-test.

F Surface plasmon resonance analysis of KLC2 binding to biotinylated R4 peptide. Recombinant KLC2 was injected at different concentrations (5-160 nM) on biotinylated R4 or N4 peptides immobilized to a streptavidin sensor chip. The dissociation steady-state constant, KD, was determined by fitting the sensogram to a 1:1 model.

G Kinetic analyses of photoconverted Dendra fusion proteins in cultured DRG neuron axons. Adult mouse DRG neurons were transfected by electroporation with constructs expressing HA-Dendra-GAR(WT)—wild-type nucleolin GAR domain N-terminally fused with HA-Dendra, or HA-Dendra-GAR(N) with 10 arginines in the GAR domain mutated to asparagines. 48 h after plating and transfection, Dendra fluorescence was photoconverted using a DMD module to restrict conversion within the cell body. Time-lapse images were collected from the entire field of view, and red signal intensity was analyzed within axons at distances of 60–90 μm from the cell body. Photoconverted signal sampled at 10 s intervals is shown, normalized to signal intensity before photoconversion. $n = 3$ biological repeats comprising 7 cells each. Means ± SEM; $^{****}P < 0.0001$ (ANOVA).

See also Appendix Fig S2.
Source data are available online for this figure.

2018). We therefore examined whether the GAR domain of nucleolin can bind the AS1411 aptamer and tested its role in axonal, plasma membrane, and nucleolar localization of nucleolin. Here, we show that the GAR domain drives nucleolin localization to all these subcellular compartments by distinct mechanisms, and present evidence from a gene-edited mouse model that the GAR domain is critical for axonal trafficking of mRNA by nucleolin and for its effects on neuronal growth.

Results

Nucleolin–kinesin interactions are mediated by the GAR domain

We first tested whether the nucleolin GAR domain binds AS1411. Synthetic peptides corresponding to different segments of the nucleolin GAR domain (Fig 1A and Appendix Fig S1A) were tested for AS1411 binding by ELISA (Appendix Fig S1B). The AS1411 aptamer, but not the control DNA, showed binding to 22–28 residue peptides derived from N-terminal, middle, and C-terminal segments of the GAR domain (Appendix Fig S1C). We further narrowed our testing to sequences of 15 or 18 residue peptides (designated R3 or R4, respectively) and designed corresponding R-to-A (A3) or R-to-N (N4) control peptides. AS1411 bound to these shorter GAR-derived peptides but not the controls (Fig 1B and Appendix Fig S1C). We then assessed the spectrum of GAR interactors by using biotinylated versions of the R3 versus A3 peptides as baits for pulldowns from mouse sciatic nerve axoplasm, identifying co-precipitating proteins by mass spectrometry (MS). The data were analyzed using SAINTexpress (Teo *et al*, 2014), and a total of 352 candidate interacting proteins were identified (Table EV1, Fig EV1).

Interestingly, we identified 16 kinesin complex components, comprising motors and adaptors from four kinesin subfamilies that

Figure 3. GAR domain interactions with phospholipid membranes.

A Molecular dynamics simulations of native (R4) or variant (K4 and N4) nucleolin GAR-derived peptides interacting with an idealized phospholipid bilayer (phosphatidylcholine (PC): phosphatidylserine (PS), 4:1) in water. Amino acid sequences of peptides are shown above. Shaded area—standard deviations of three independent runs, each 50 ns long. Mean values are indicated by colored lines, and overlay of these is shown on the right.

B Flow cytometry histograms of TAMRA-labeled peptide uptake into HEK-293 cells after 1-h incubation at 4°C in growth medium.

C Quantification of mean fluorescence intensities in (B). $n = 6$ independent biological repeats; means ± SEM; $^{*}P < 0.05$, $^{***}P < 0.001$, $^{****}P < 0.0001$, ANOVA with Tukey's post-test.

D Uptake of TAMRA-labeled R4 and N4 peptides into cultured DRG neurons. Cells were incubated with peptides dissolved to 5 μM in growth medium for 30 min at 4°C, washed, fixed, and analyzed by confocal microscopy. PC—phase contrast. Scale bar—10 μm.

E Quantification of (D). $n = 3$ independent biological repeats; means ± SEM; $^{*}P < 0.05$, paired Student's t-test a. u. – arbitrary units.

F Analysis of cell surface nucleolin in HEK-293 cells. Cells were treated with 0.5 mM sulfo-NHS-SS-biotin for 30 min at 4°C, lysed, and subjected to affinity pulldown of biotinylated proteins with streptavidin Dynabeads, eluted by 50 mM DTT, and probed in Western blot with antibodies indicated on the left. Endogenous nucleolin (Ncl) was readily detected in the biotinylated membrane protein pool. Glyceraldehyde 3-phosphate dehydrogenase (GAPDH) and importin β1 (Impβ1) served as negative controls.

G HEK-293 cells were transfected with plasmids expressing HA-Dendra2-full-length nucleolin (Ncl FL), HA-Dendra2-nucleolin with a GAR domain deletion (Ncl ΔGAR), or HA-Dendra2-nucleolin with all 10 arginines in the GAR domain mutated to asparagines (Ncl GAR(N)) and processed as in (F).

H Quantification of (G). Levels of nucleolin in pulldowns were normalized to input levels and expressed as % relative to full-length HA-Dendra2-nucleolin. $n = 4$ independent biological repeats; means ± SEM; $^{****}P < 0.0001$, ANOVA with Dunnett's post-test.

See also Fig EV2 and Appendix Fig S3.
Source data are available online for this figure.

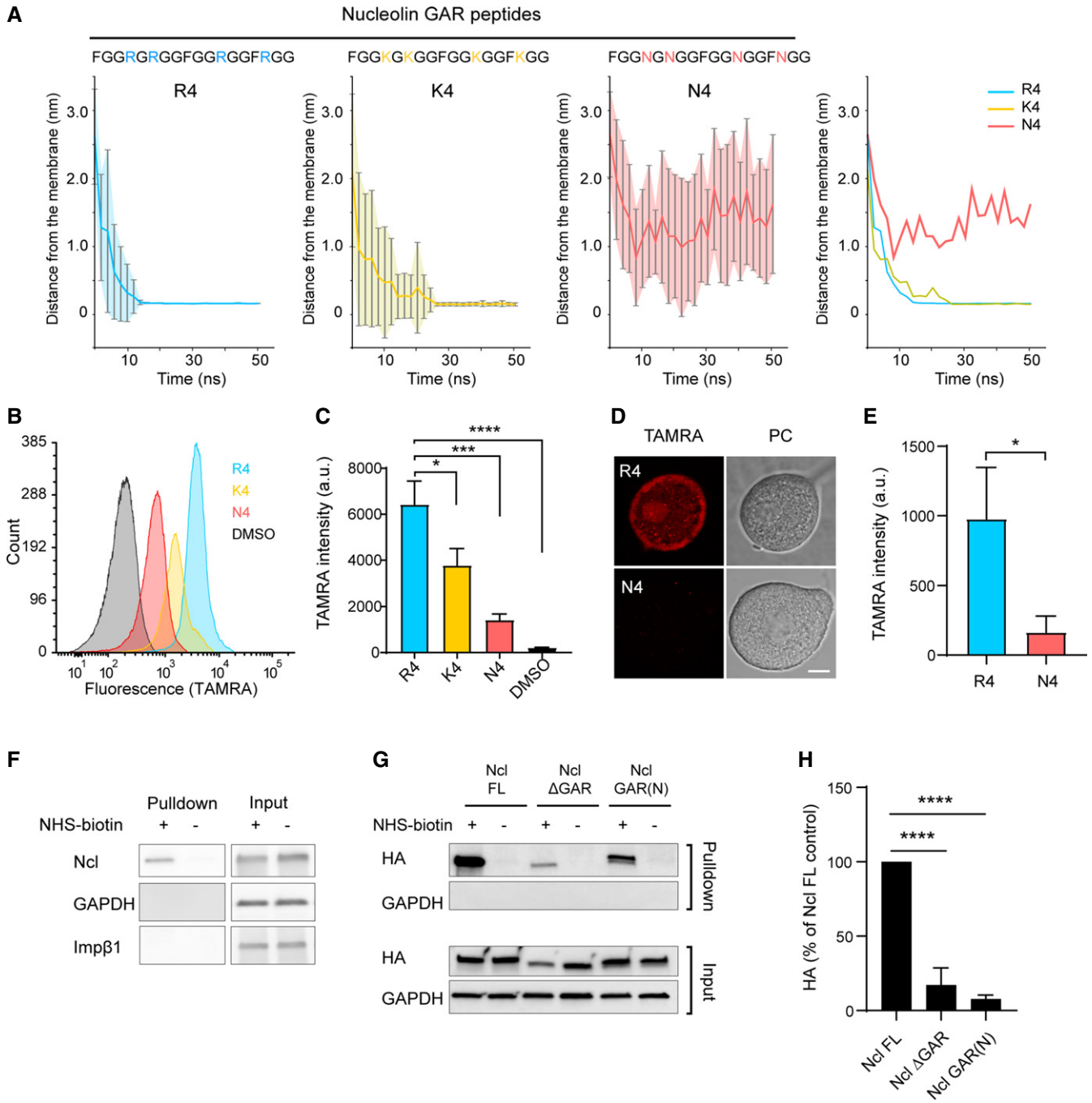

Figure 3.

transport a variety of axonal cargos (Fig 1C). We chose to validate the interaction for Kif5a, a motor component of the kinesin 1 complex, since we had previously shown that the Kif5a complex associates with nucleolin, and that this association is reduced by the AS1411 aptamer (Perry *et al*, 2016). Indeed, affinity purification followed by automated capillary Western blotting showed that both R3 and R4 peptides associated with Kif5a, while their A3 and N4 controls did not (Fig 1D–F). The requirement for the nucleolin GAR domain in kinesin binding was further confirmed by co-immunoprecipitation analyses of Kif5a with HA-Dendra2-tagged nucleolin constructs expressed in HEK-293 cells. Both GAR domain deletion and substitution of all ten arginines in the GAR domain by asparagines (henceforth termed GAR(N)) significantly reduced co-precipitation of Kif5a with nucleolin (Fig 2A and B). Moreover, the R4 peptide, but not its N4 control, acted as a dominant-negative by significantly perturbing endogenous Kif5a-nucleolin interaction in sciatic nerve axoplasm, as shown by reduction in their co-immunoprecipitation (Fig 2C–E). We then set out to test direct binding of GAR-derived peptides with kinesin complex components, using surface plasmon resonance to assess binding of R4 versus N4

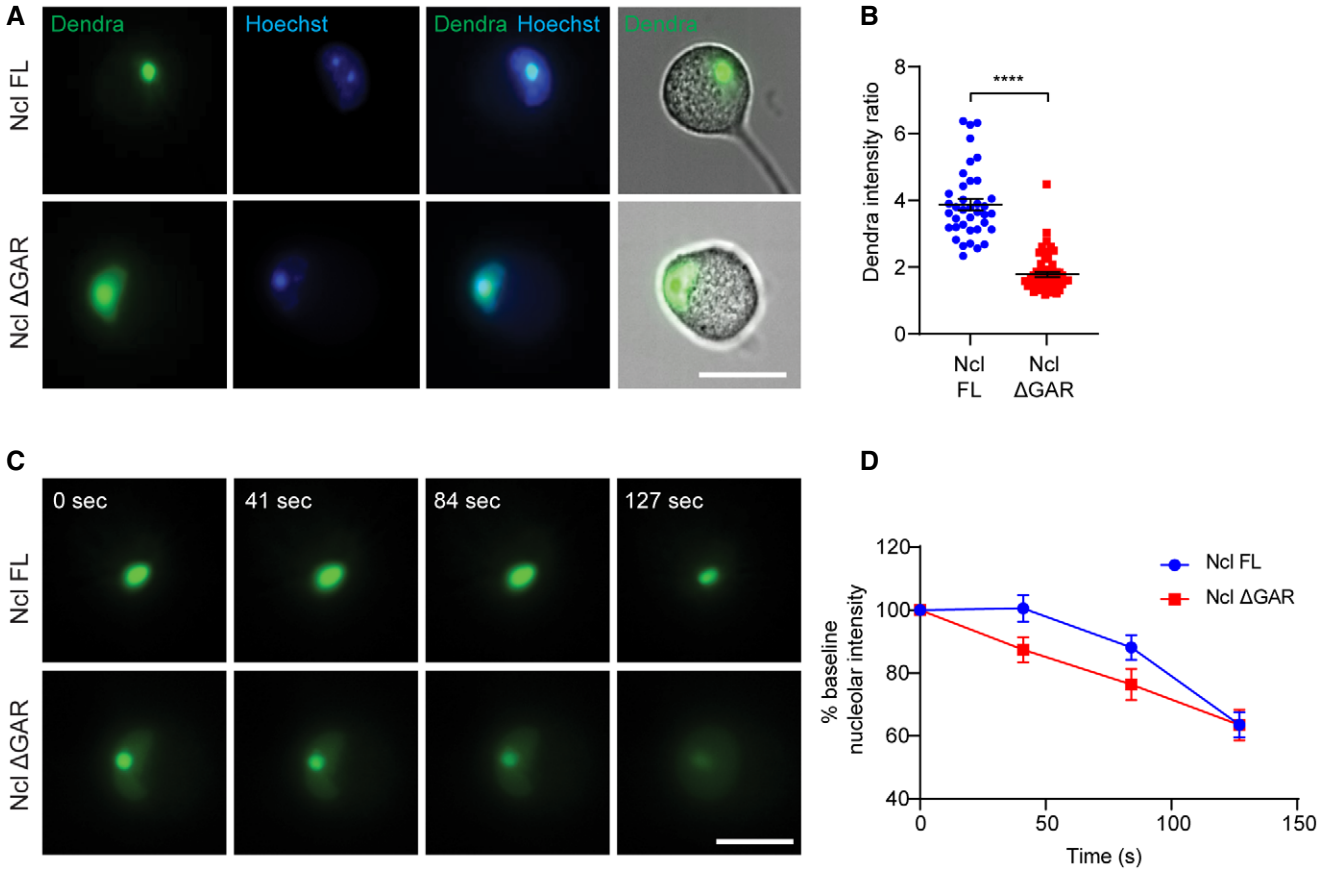

Figure 4. GAR domain and nucleolar localization of nucleolin.

A GAR deletion in nucleolin reduces partitioning to nucleoli in adult DRG neurons, transduced with the peripheral neuron-specific AAV-PHP.S vector expressing full-length HA-Dendra2-nucleolin (Ncl FL) or respective ΔGAR mutant (Ncl ΔGAR) upon seeding, and analyzed by epifluorescence microscopy 9–10 days later. Shown are representative Dendra2 fluorescence images collected from the non-activated (green) emission line. Hoechst 33342 (10 μM) was used to outline nuclei. Superimposed phase contrast and Dendra2 fluorescence images are shown on the right. Scale bar—25 μm.

B Quantification of the nucleolar/nuclear intensity ratios in DRG cells shown in (A). n = 38–54 cells per sample in three independent biological repeats; means ± SEM; ****P < 0.0001, Mann–Whitney test.

C Time-lapse live imaging of nuclei in DRG neurons transduced with AAV-PHP.S HA-Dendra2-nucleolin (full-length and ΔGAR mutant), after a hypotonic challenge with double-distilled water (ddH20). Shown are epifluorescence images (Dendra2 green emission line) taken at indicated times after medium replacement with ddH20. Scale bar—10 μm.

D Quantification of nucleolar Dendra2 signal in (C) with intensity values immediately before medium replacement set as 100%. n = 17–24 cells per sample in three biological repeats; means ± SEM; two-way ANOVA with Sidak's post-test detected a significant time-dependent reduction in nucleolar signal (P < 0.0001) and no difference between full-length and ΔGAR mutant nucleolin (P > 0.05).

See also Appendix Fig A4.

peptides with kinesin light chain 2 (KLC2) and with Kif5c. While there was no specific binding of the GAR-derived peptides to Kif5c; R4, but not the N4 control, bound KLC2 with a K_d of 57.9 nM (Fig 2F). Recent work has linked transport of RBP-mRNA complexes in association with endosomes and lysosomes (Cioni *et al*, 2019; Liao *et al*, 2019). However, we do not find the lysosome/endosome marker LAMP1 in Kif5a-Ncl coprecipitates (Appendix Fig S2). Finally, we tested axonal localization of GAR domain constructs by monitoring appearance of axonal signal after photoconversion of fluorescent dendra protein fusions in the cell bodies of cultured dorsal root ganglia (DRG) neurons. We observed a significant time-dependent increase in photoconverted dendra-GAR(WT), but not dendra-GAR(N), in distal axons of the transfected neurons (Fig 2G). Taken together, these findings support a critical role for the GAR domain in nucleolin interaction with kinesin complexes and in axonal localization.

Nucleolin localization to the plasma membrane is facilitated by the GAR domain

Nucleolin has also been reported to reside at the plasma membrane (Bates *et al*, 2017) and indeed, an appreciable fraction of the GAR protein interactors we identified are membranal (Fig EV1). Although nucleolin lacks any obvious membrane interaction domains or motifs, arginine-rich peptides are known to penetrate cellular membranes (Allolio *et al*, 2018; Vazdar *et al*, 2018), raising the possibility that the arginine-rich GAR domain might enable nucleolin association with the plasma membrane. We performed

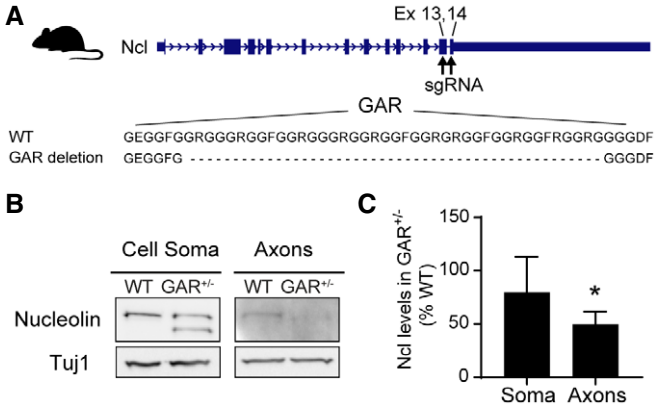

Figure 5. Reduced levels of axonal nucleolin in nucleolin GAR$^{+/-}$ mice.

A Targeted deletion of nucleolin GAR domain by CRISPR-Cas9. Schematic shows mouse nucleolin exons targeted by single guide RNAs (sgRNAs) and resulting deletion in the GAR domain amino acid sequence.

B Western blot analysis of nucleolin in DRG neurons from wild-type (WT) and GAR$^{+/-}$ mice cultured in Boyden chambers. Tuj1 was used as a loading control. The higher nucleolin band in GAR$^{+/-}$ corresponds to WT nucleolin and lower band to nucleolin with a 41 aa deletion (corresponding to about 4 kDa reduction in protein size).

C Quantification of (B), total nucleolin levels (sum of both bands where applicable) were normalized to Tuj1 and expressed as GAR$^{+/-}$ / WT ratios. $n = 3$ independent biological repeats; means ± SEM; *$P < 0.05$, 1 sample t-test.

See also Appendix Fig S5.
Source data are available online for this figure.

molecular dynamics simulations to explore this possibility, examining the propensity of GAR-derived peptides to interact with an idealized phospholipid bilayer. Specifically, we compared simulated membrane association of the R4 GAR peptide with those of lysine (K4) or asparagine (N4) substitutions for the arginines in this sequence. As shown in Figs 3A and EV2, both the R4 and K4 peptide simulations showed robust membrane association, while the N4 did not. Membrane contacts of the charged peptides were primarily driven by arginine and phenylalanine residues in the case of the R4 peptide, while phenylalanines predominated for the K4 (Fig EV2C).

Experimental confirmation for membrane penetration by R4 and K4 peptides was obtained by FACS analyses of HEK-293 (Fig 3B and C) and U937 (Appendix Fig S3A and B) cells incubated with fluorescently labeled peptides for 1 h at 4°C. The R4 peptide entered the cells at higher efficiency than either K4 or N4 peptide. Similar results were obtained for R4 versus N4 peptides on DRG neuron cultures assessed by confocal microscopy (Fig 3D and E). We then proceeded to assess plasma membrane association of endogenous nucleolin by cell surface biotinylation in HEK-293 cells, first validating the assay by demonstrating membrane expression of a G protein-coupled inwardly rectifying potassium channel (Appendix Fig S3C). Endogenous nucleolin was readily detected in the biotinylated membrane protein pool (Fig 3F). The role of the GAR domain in cell surface association of nucleolin was assessed in HEK-293 cells transfected with native nucleolin versus GAR domain deletion or GAR(N) mutants. Deletion or mutation of the GAR domain greatly reduced cell surface association of nucleolin (Fig 3G and H). However, both wild-type GAR and the GAR(N) mutant showed comparable membrane localization when expressed as single domains (Appendix Fig S3D and E). Taken together, these experiments support a role for the GAR domain in plasma membrane interactions of nucleolin and further suggest that membrane interactions can be influenced by the context of the domain in the protein.

GAR and nucleolar localization of nucleolin

The findings above support roles for the GAR domain in motor-driven transport of nucleolin and in plasma membrane interactions, but the main pool of nucleolin in cells is nucleolar, and previous reports had suggested that the GAR domain is required for nucleolar localization (Pellar & DiMario, 2003). We therefore asked to what degree the GAR domain influences accumulation or retention of nucleolin in the nucleolus. Transfection with Dendra2 fusions of full-length or GAR deletion nucleolin revealed reduced partitioning of GAR-deleted nucleolin to the nucleolus, albeit to different degrees in different cell types (Fig 4A and B, Appendix Fig S4A–D). Disruption of liquid–liquid phase separation (LLPS) by hypotonic challenge with ddH_2O (Nott *et al*, 2015) reduced nucleolin in nucleoli (Fig 4C and D, Appendix Fig S4E–H), with very similar kinetics for full-length and GAR deletion constructs in both DRG neurons and N2a cells. Significant differences between full-length and GAR deletion nucleolin were observed only in HEK-293 cells (Appendix Fig S4). Taken together, these data indicate that GAR-deleted nucleolin is still found mainly in the nucleus, with somewhat less pronounced

Figure 6. Reduced levels of nucleolin-mRNA cargos in axons of nucleolin GAR$^{+/-}$ mice.

A, B Representative maximum projections of exposure-matched confocal images of immunofluorescence for nucleolin and neurofilament (NF) and the neuronal marker Tuj1 in sciatic nerve axons from WT and GAR$^{+/-}$ mice shown in (A). Upper panels show total nucleolin stain. Middle panels show merged image of nucleolin (gray), NF and Tuj1 (magenta), and DAPI (blue). Lower panels show nucleolin overlaps with NF and Tuj1 signals as the "axon only" signal. B shows quantification of nucleolin immunofluorescence with approximately a 50% reduction in nucleolin in the axons of GAR$^{+/-}$ mice *in vivo*. $n = 3$ WT, $n = 4$ GAR$^{+/-}$; means ± SEM; *$P < 0.05$, unpaired Student's t-test. Scale bar – 10 μm.

C–F Representative, exposure-matched maximum projection confocal images of FISH for *Kpnb1* (C) or *mTOR* (E) mRNA and NF plus Tuj1 immunostaining from sciatic nerve sections from WT (left) or GAR$^{+/-}$ mice. Upper panels for each show total mRNA signal. Middle panels show mRNA (gray) signals merged with NF plus Tuj1 (magenta) and DAPI (blue). Lower panels show mRNA signal that overlap with NF plus Tuj1 signal (labeled "axon only" signal). Quantification of axonal *Kpnb1* (D) and *mTOR* (F) mRNA signals compared to the negative control, *DapB* mRNA, show a significant reduction in these axonal mRNAs in the GAR$^{+/-}$ mice. $n = 3$ WT, $n = 3$ GAR$^{+/-}$; means ± SEM; **$P < 0.01$, ***$P < 0.001$, ****$P < 0.0001$ unpaired Student's t-test. Scale bar – 10 μm.

See also Appendix Fig S6.

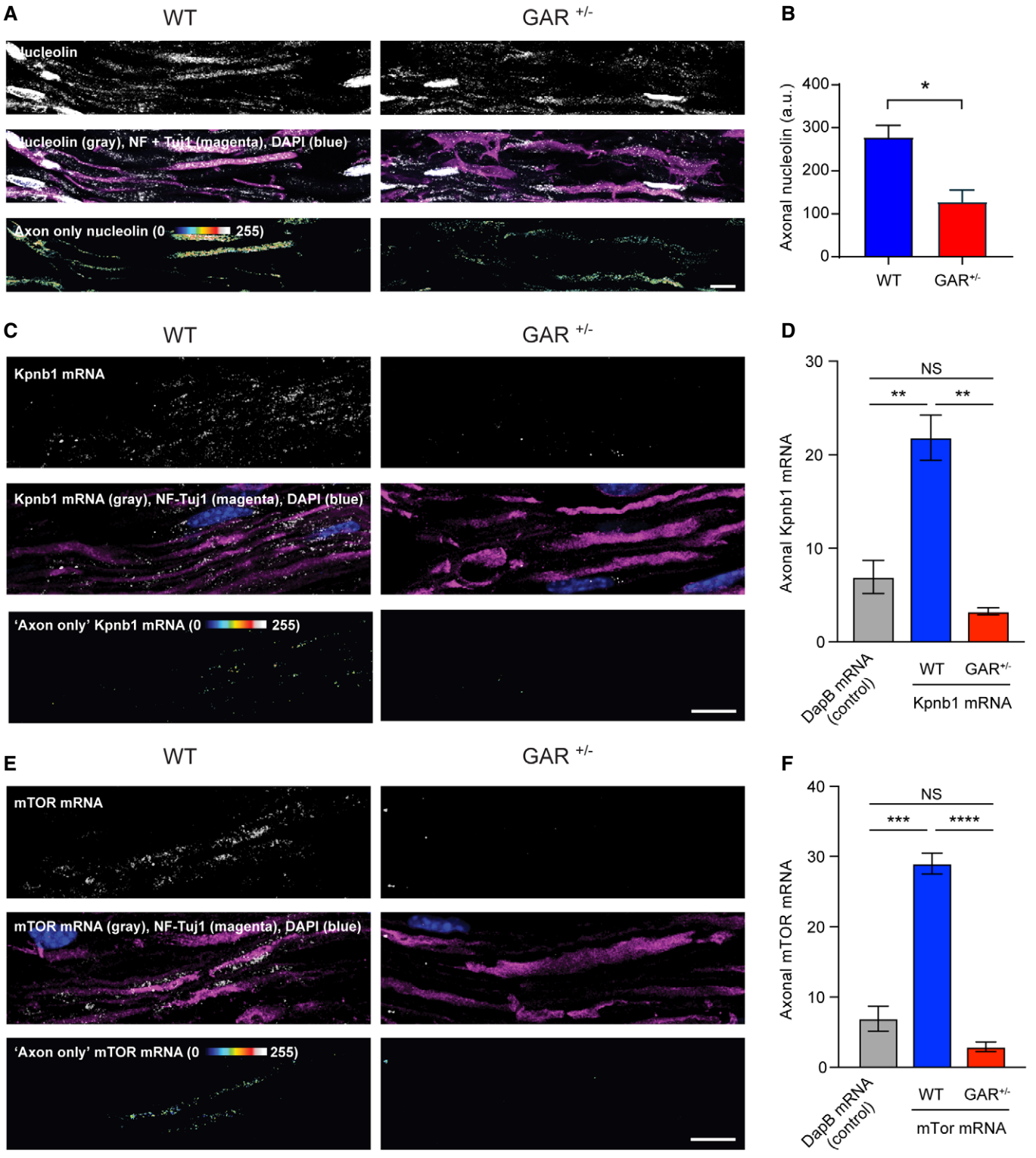

Figure 6.

nucleolar segregation. Thus, the GAR domain contributes to nucleolin partitioning to nucleoli, but other domains of nucleolin such as the RNA recognition motifs (Okuwaki *et al*, 2020) likely have a more dominant role in the LLPS-dependent processes that form and stabilize nucleoli.

GAR domain deletion perturbs mRNA localization

In order to study the *in vivo* implications of perturbing GAR-mediated nucleolin subcellular localization, we generated a GAR deletion mouse line by CRISPR/Cas9 gene editing, using two

sgRNAs flanking the GAR domain (Fig 5A). Four of the several founder mice generated were subsequently outbred on two genetic backgrounds; however, no F1 mice homozygous for the GAR deletion were identified from any of the founder lines. Genotyping of more than 30 E10.5 embryos from timed pregnant females revealed that there were no homozygous embryos, suggesting that biallelic deletion of the nucleolin GAR domain is lethal at early stages of development (Appendix Fig S5). Thus, subsequent analyses were conducted on animals heterozygous for the GAR deletion in nucleolin.

We first cultured DRG neurons from GAR$^{+/-}$ mice in modified Boyden chambers, allowing subsequent protein extraction from axons and cell bodies separately. Western blot quantification of nucleolin extracted from the cell soma compartment clearly showed that the mutant GAR deletion protein is expressed, while similar analysis of the axonal compartment revealed marked reduction in

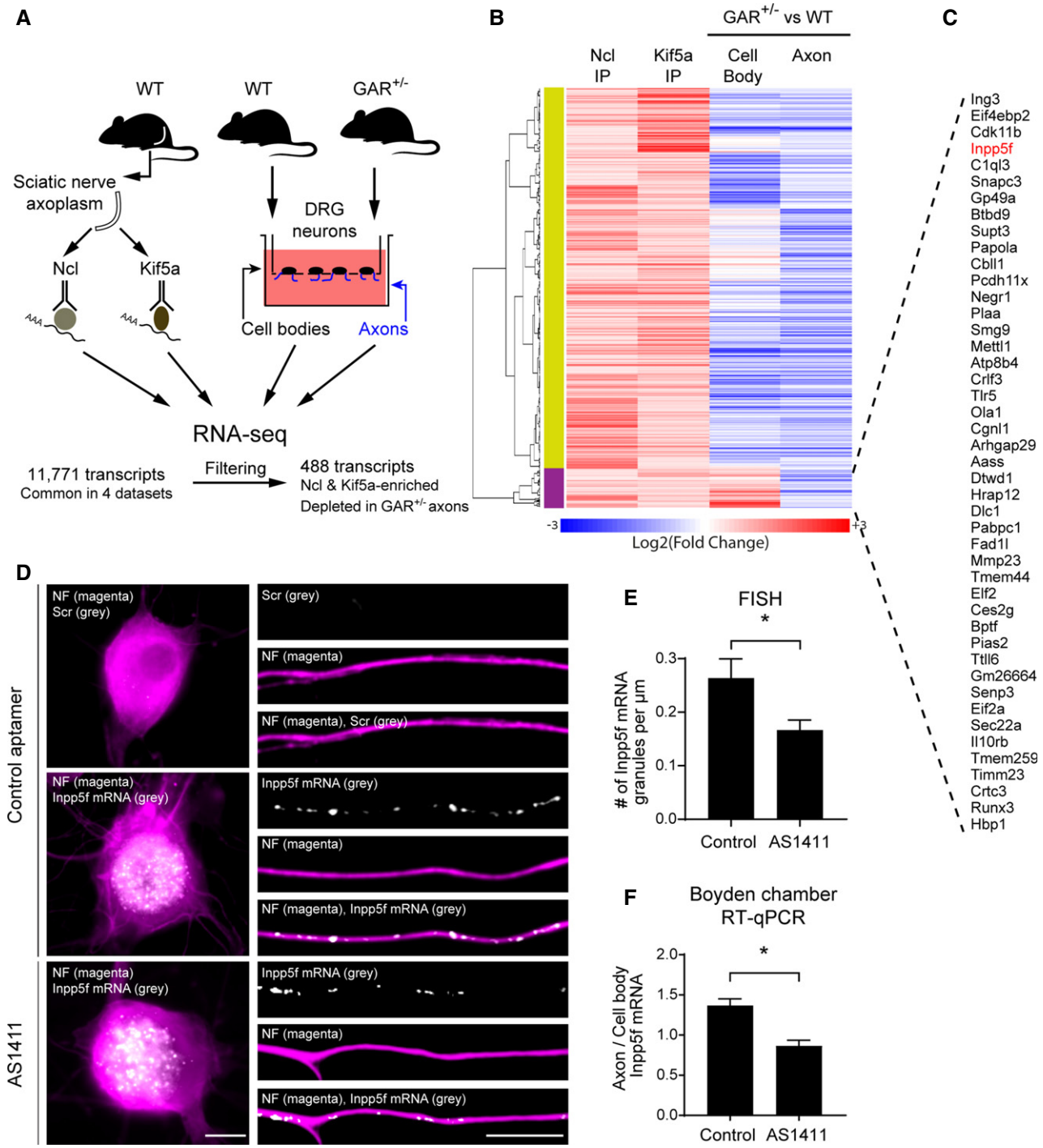

Figure 7.

Figure 7. Axonal mRNAs associated with the Ncl-Kif5a complex.

A Workflow for profiling mRNAs bound by the Ncl-Kif5a complex. Nucleolin (Ncl) and Kif5a-binding RNAs were isolated from wild-type (WT) adult mouse sciatic nerve axoplasm by immunoprecipitation; in addition, DRG neurons from adult WT and $GAR^{+/-}$ mice were cultured in modified Boyden chambers and RNA was isolated from cell body and axonal sides. RNA-seq analysis from the resulting four datasets yielded 11,771 overlapping transcripts. The latter were further processed into a subset of 488 transcripts enriched in Ncl and Kif5a pulldown and depleted in axons of nucleolin $GAR^{+/-}$ mice compared with WT (B). Please see Fig EV3 for a detailed workflow.

B Clustering of 488 Ncl/Kif5a-enriched transcripts reduced in $GAR^{+/-}$ versus WT axons. Yellow cluster— transcripts not significantly enriched in the soma of $GAR^{+/-}$ DRG neurons versus the WT control, Purple cluster—transcripts enriched in the soma of $GAR^{+/-}$ DRG neurons versus the WT control. Heatmap shows mean log2-fold changes across four datasets (see also Fig EV3A), from left to right: (i) nucleolin-binding mRNAs in mouse sciatic nerve axoplasm; (ii) Kif5a-binding mRNAs in mouse sciatic nerve axoplasm; (iii) mRNA abundance in DRG neuron cell bodies of $GAR^{+/-}$ mice relative to abundance in WT mice; and (iv) mRNA abundance in DRG neuron axons of $GAR^{+/-}$ mice relative to abundance in wild-type mice. All transcripts chosen for this cluster analysis showed significant enrichment in Ncl IP and reduction in $GAR^{+/-}$ axons versus WT, as determined by rank–rank hypergeometric overlap (RRHO) as well as a fold change in Kif5a IP versus control > 2.

C Genes comprising the purple cluster—transcripts significantly enriched by both Ncl and Kif5a immunoprecipitation and showing a reduction in $GAR^{+/-}$ axons concurrent with an enrichment in $GAR^{+/-}$ soma (compared to the WT control). Inpp5f (highlighted in red) was chosen for follow-up.

D Representative images for FISH analysis of *Inpp5f* in DRG neurons treated for 48 h with 10 μM AS1411 or 10 μM control aptamer, replated, and grown for 18 h. FISH signal is shown in gray; cell somata (left) and axons (right) are visualized by neurofilament immunostaining (magenta). Scr—scrambled FISH probe served as a negative control. Scale bar—10 μm.

E Quantification of axonal *Inpp5f* signal in (D) as density of RNA granules along axons. n = 11–19 cells per sample; means ± SEM; $^*P < 0.05$, unpaired Student's t-test.

F RT–qPCR analysis of axonal *Inpp5f* mRNA levels in DRG neurons grown in Boyden chambers and treated for 48 h with 10 μM AS1411 or 10 μM control aptamer. Axon/cell body ratios of *Inpp5f* normalized to *Gapdh* levels are shown. n = 4 independent biological repeats; means ± SEM; $^*P < 0.05$, unpaired Student's t-test.

See also Fig EV3.

the deletion mutant band and a concomitant reduction in total nucleolin levels in the axon (Fig 5B and C). Immunostaining of longitudinal sections from sciatic nerves of wild-type and $GAR^{+/-}$ mice revealed a similar reduction in axonal nucleolin in the mutant animals (Fig 6A and B). *Kpnb1* (Importin β1) and *mTOR* mRNAs are known cargos of nucleolin (Perry *et al*, 2016; Terenzio *et al*, 2018); hence, we examined levels of these mRNAs by single molecule fluorescence *in situ* hybridization (FISH) on longitudinal sections of sciatic nerve from the same animals. These FISH analyses showed significant reductions in axonal levels of both *Kpnb1* and *mTOR* mRNAs in $GAR^{+/-}$ axons *in vivo* (Fig 6C–F and Appendix Fig S6A). Thus, the GAR domain is required for axonal localization of nucleolin and its cargo mRNAs *in vivo*.

In order to further characterize the mRNA cargos that depend on nucleolin for axonal localization, we performed RNA sequencing on pulldowns of nucleolin or Kif5a from sciatic nerve axoplasm, and on RNA extracted from isolated axons of wild-type or $GAR^{+/-}$ sensory neurons cultured in Boyden chambers (Figs 7A and EV3). Of the close to 12,000 RNAs found in these datasets, 488 were enriched in nucleolin and Kif5a pulldowns and were also depleted from $GAR^{+/-}$ versus wild-type axons (Figs 7A and B, and EV3, Table EV2). From the latter, 45 mRNAs were enriched in the soma of $GAR^{+/-}$ neurons (purple cluster in Fig 7B and C), hence are likely mislocalized due to subcellular changes in nucleolin localization. One of these mRNAs, *Inpp5f* (also known as Sac2), encodes a polyphosphoinositide phosphatase that was reported to regulate both cardiac cell and neuronal growth (Zhu *et al*, 2009; Zou *et al*, 2015) and was therefore selected for validation. We tested *Inpp5f* mRNA dependence on nucleolin for localization to axons by FISH on sensory neurons challenged with the AS1411 aptamer, which perturbs nucleolin localization to axons (Perry *et al*, 2016). Indeed, AS1411-treated neurons revealed a significant reduction in axonal *Inpp5f* mRNA as compared to control aptamer treatments (Fig 7D and E). Similar reduction in axonal *Inpp5f* mRNA was detected by qPCR analysis in sensory neurons grown in Boyden chambers (Fig 7F).

To more directly test the requirement for nucleolin's GAR domain in axonal localization of cargo mRNAs, we asked if the loss of cargo mRNAs from axons with depletion of nucleolin can be reversed by nucleolin wild-type versus nucleolinΔGAR protein expression. For this, endogenous nucleolin was depleted from adult DRG neurons using siRNA targeting the 3′UTR of nucleolin mRNA. These neurons were then transfected with siRNA-resistant nucleolin and nucleolinΔGAR expression constructs, and cell body and axonal levels of nucleolin cargo mRNAs were assessed by FISH. Endogenous nucleolin mRNA and protein were significantly reduced by siRNA knockdown (Appendix Fig S7). Nucleolin-depleted neurons transfected with si-resistant full-length nucleolin showed comparable levels of *Kpnb1*, *mTor*, and *Inpp5f* mRNAs to the control siRNA-transfected neurons, both in axons and in cell body. In contrast, nucleolin-depleted neurons transfected with si-resistant nucleolinΔGAR showed significantly lower *Kpnb1*, *mTor*, and *Inpp5f* mRNA levels in axons (Figs 8A–D, EV4, and EV5). Together, these data support an essential role of the GAR domain in nucleolin-dependent transport of axonal mRNAs.

GAR mutant neurons exhibit increased growth

The findings summarized above establish the GAR domain as a critical determinant of nucleolin localization to axons and show that GAR domain deletion perturbs axonal localization of nucleolin cargo mRNAs important in growth regulation. Our previous studies have shown that axonal depletion of motor proteins, RNA-binding proteins, and mRNAs implicated in this growth controlling pathway have all caused acceleration of axonal growth (Rishal *et al*, 2012; Perry *et al*, 2016), as predicted by our previously proposed cell length sensing model (Albus *et al*, 2013; Rishal & Fainzilber, 2019). Indeed, time-lapse imaging of sensory neuron growth in culture revealed accelerated growth of $GAR^{+/-}$ neurons as compared to their wild-type counterparts (Fig 9A and B). We sought to further corroborate this finding by the expression of an HA-Dendra-GAR fusion construct as a dominant-negative that should compete with endogenous nucleolin for access to the axon. Indeed, the expression of the wild-type GAR domain enhances axon growth as compared to expression of a mutant GAR wherein all arginines are substituted by asparagines (Fig 9C and D). Thus, perturbation of GAR-mediated axonal localization of nucleolin enhances axon growth, as predicted

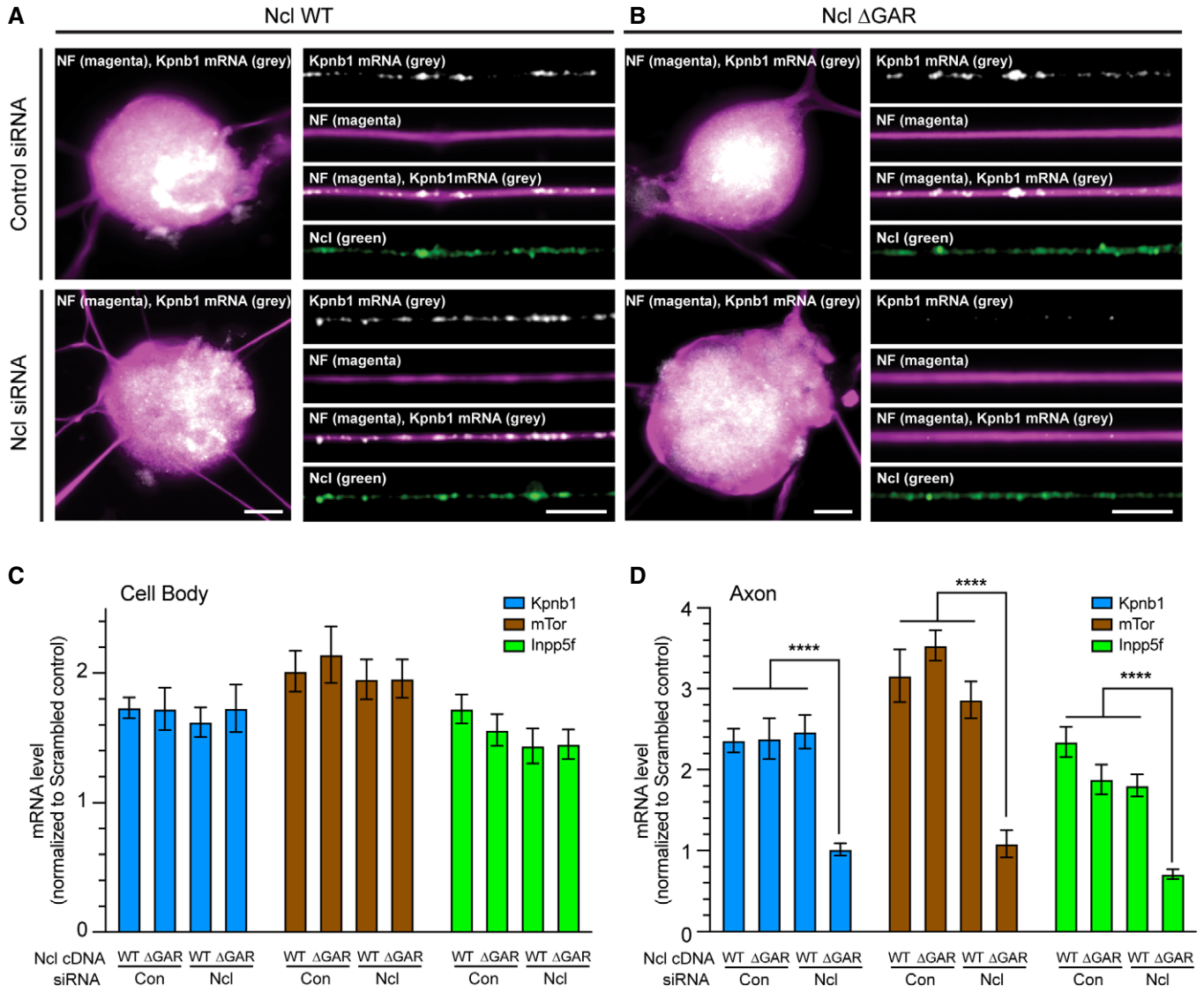

Figure 8. Wild-type, but not ΔGAR mutant nucleolin, rescues defective axonal localization of its cargo mRNAs in DRG neurons treated with nucleolin siRNA.

A, B Representative exposure-matched FISH/IF images for DRG neurons cotransfected with control versus nucleolin (Ncl) siRNA plus siRNA-resistant wild-type (WT; A) or ΔGAR (B) Ncl cDNAs. Axonal Kpnb1 mRNA is decreased with the Ncl knockdown, and this is not rescued by expression of ΔGAR Ncl mutant (scale bars—10 μm).

C, D Quantification of RNA signals from FISH/IF for *Kpnb1, mTOR, and Inpp5f* in cell bodies (C) and axons (D) for DRG cultures transfected as in A are shown. Axons of neurons cotransfected with Ncl siRNA plus ΔGAR show significantly lower signals for each mRNA compared with Ncl siRNA plus WT and control siRNA plus WT or ΔGAR; $N \geq 10$ for cell bodies, $N \geq 25$ for axons over 3 biological repeats; means ± SEM; ****$P \leq 0.001$ by one-way ANOVA with Tukey HSD post hoc.

See also Figs EV4 and EV5, and Appendix Fig S7

by the length sensing model (Rishal & Fainzilber, 2019) and our previous findings (Rishal *et al*, 2012; Perry *et al*, 2016).

Discussion

Our findings establish the GAR domain as a key determinant of nucleolin subcellular localization, most prominently directing its transport on kinesin motors to cytoplasmic extremities of the cell (Fig 10). In addition to associating with kinesin motor complexes, the GAR domain also enables nucleolin association with the plasma membrane and contributes to maintaining nucleolin within the nucleolus, a canonical membraneless organelle. Of note, we cannot rule out that the defects in nucleolar dynamics of nucleolin caused by GAR domain deletion contribute to the axonal localization and cell growth phenotypes, although the bulk of our evidence suggests that membrane and axonal localization roles are more prominent than nucleolar effects of GAR removal. The versatile roles of the GAR domain are reflected in the fact that deletion of this small domain in the mouse causes embryonic lethality. An early study had shown that a complete knockout of nucleolin was lethal to chicken lymphoblast DT40 cells (Storck *et al*, 2009), and it is striking that removal of such a small domain in this large protein is lethal *in vivo*.

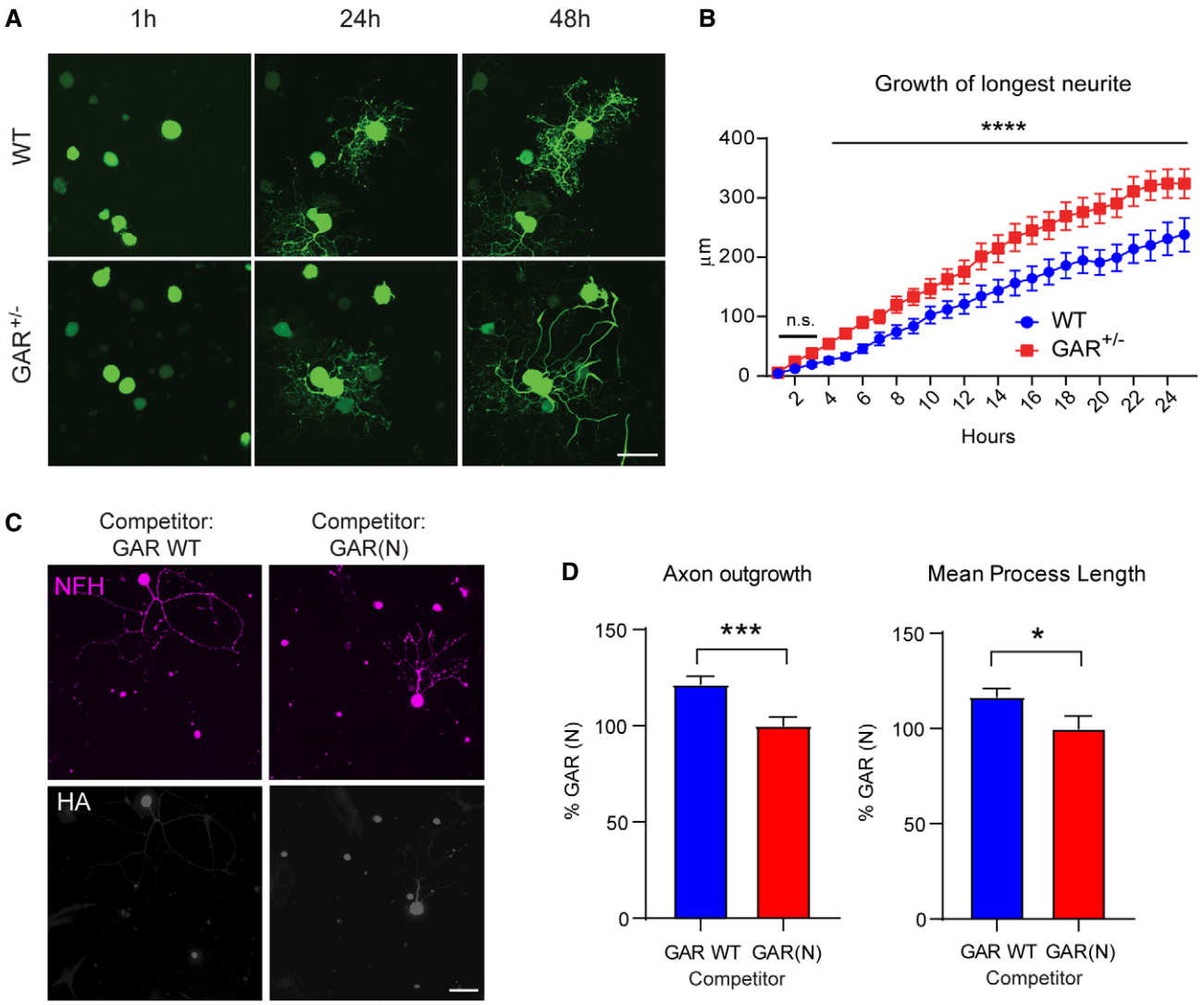

Figure 9. Reduced levels of full-length axonal nucleolin increase axonal outgrowth in DRG neurons.

A Cultured DRG neurons from wild-type (WT) Thy1-YFP mice and Thy1-YFP / GAR$^{+/-}$ mice (YFP signal is shown in green). Cells were imaged every hour for a period of 48 h. Scale bar—100 µm.

B Quantification of the time-lapse imaging experiment shown in (A). Growth rate of the longest neurite of each cell was calculated from the time point of starting growth. $n = 4$ independent biological repeats; means ± SEM, ****$P < 0.0001$, two-way ANOVA.

C Fluorescence images of cultured DRG neurons from adult C57BL/6 mice infected with AAV-PHP.s expressing HA-Dendra fused with the wild-type nucleolin GAR domain (GAR WT) or with the GAR domain with all 10 arginines substituted with asparagines, GAR(N). Neurons were replated 9–10 days after AAV infection. 24 h after replating, cells were fixed and stained with anti-HA (gray) and anti-NFH (magenta) antibodies. Scale bar—100 µm.

D Quantification of total axonal outgrowth and mean process length in HA-positive cells in (C). Outgrowth measurements were based on NFH staining. $n = 6$ independent biological repeats; means ± SEM; *$P < 0.05$, ***$P < 0.001$ (Student's-test).

GAR domains are found in numerous mammalian RBPs, and their roles have been studied most extensively in RNA binding and in LLPS (Thandapani *et al*, 2013; Chong *et al*, 2018). Early work on nucleolin GAR focused on the contributions of this domain to nucleolar localization (Schmidt-Zachmann & Nigg, 1993; Pellar & DiMario, 2003), while more recent interest has focused on how the GAR domain influences binding of G-quadruplex RNA structures by RNA recognition motifs (RRM) in nucleolin (Masuzawa & Oyoshi, 2020; Saha *et al*, 2020). The GAR domain in FMRP was also suggested to be important for localizing G-quadruplex RNAs (Goering *et al*, 2020). Our results expand the spectrum of mechanisms employed by the GAR domain for additional versatility of functions, including plasma membrane association. Although nucleolin lacks transmembrane domains or canonical membrane anchoring motifs, substantial cell surface expression was reported in diverse cancer cells (Berger *et al*, 2015), raising the question how nucleolin interacts with membranes. We have shown that the GAR domain fulfills this function, generating membrane contacts through arginine and phenylalanine residues, and that deletion or mutation of the GAR domain reduces cell surface nucleolin. Arginine-rich peptides are

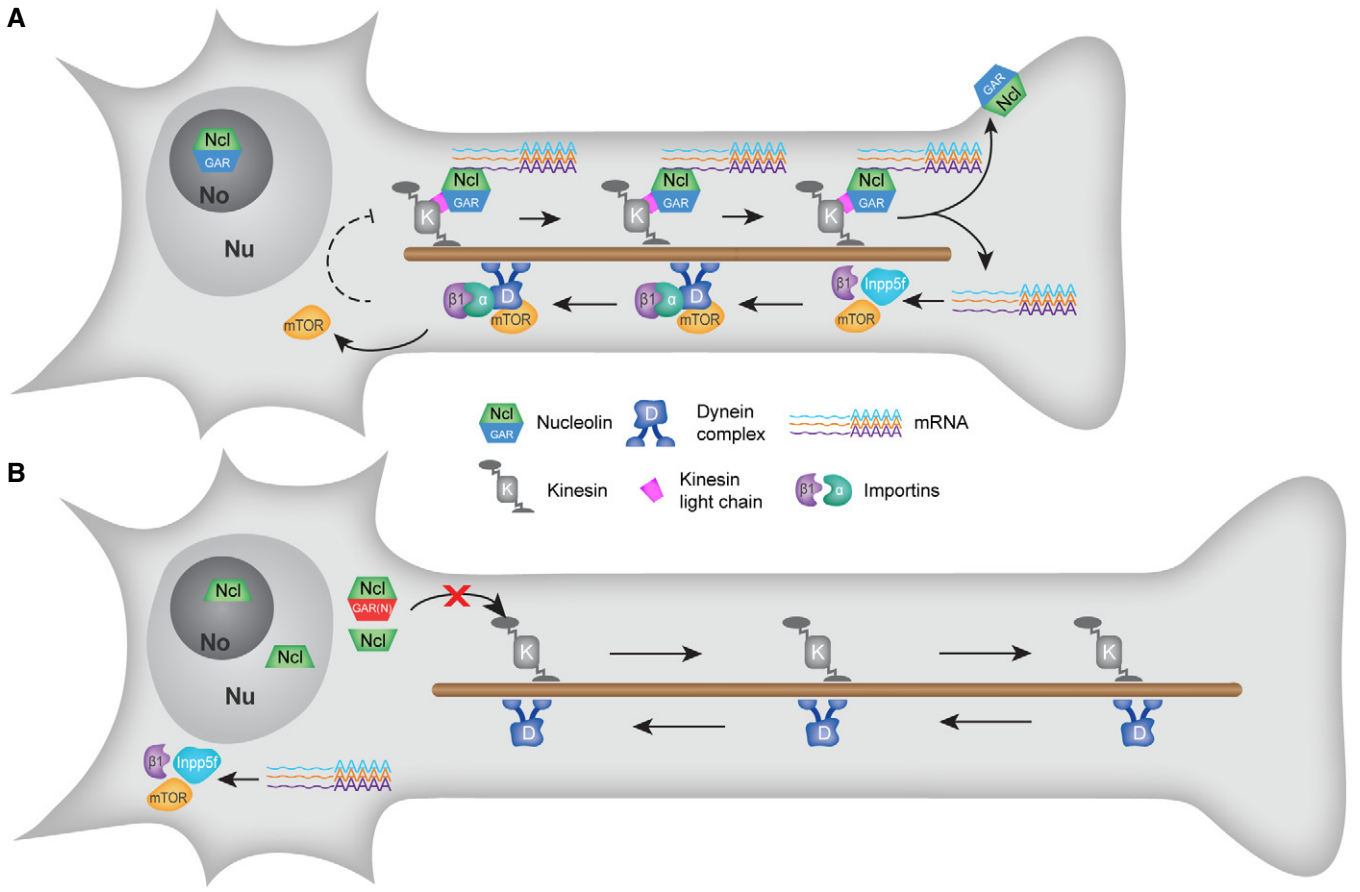

Figure 10. Essential roles for the GAR domain in subcellular localization of nucleolin.

A, B The nucleolin GAR domain binds a kinesin light chain, directly linking nucleolin–mRNA complexes to kinesin motors for axonal transport (A). The GAR domain further mediates membrane association of nucleolin. GAR-mediated subcellular targeting of nucleolin complexes enables export of key mRNAs to the axon, and the local translation of their encoded proteins for local functions in the axon, or for retrograde transport to the cell body. This reciprocal transport mechanism provides intrinsic regulation of axon length and growth, and indeed, deletion or mutation of the GAR domain (B) perturbs mRNA localization to axons and increases axonal elongation.

known to have the ability to passively penetrate cellular membranes (Takeuchi & Futaki, 2016). A number of mechanisms have been proposed for such translocation (Lamaziere *et al*, 2007; Mishra *et al*, 2011; Herce *et al*, 2014; Pae *et al*, 2014; Sun *et al*, 2014), including the induction of membrane multilamellarity and fusion (Allolio *et al*, 2018), with the first step being accumulation of arginine-rich sequence stretches at the membrane due to like-charge pairing of the guanidinium side-chain groups (Vazdar *et al*, 2018). Our data suggest that GAR domains exploit these characteristics of arginine-rich sequences to provide a novel class of membrane anchoring or membrane traversing moiety for RBPs.

Other classes of RNA granules have been shown to use membrane linkers or adapters to hitchhike on endosomes, lysosomes, or mitochondria for axonal transport (Gershoni-Emek *et al*, 2018; Cioni *et al*, 2019; Liao *et al*, 2019). In contrast, GAR-mediated transport of nucleolin is likely dependent on direct interaction of the GAR domain with kinesin complexes. Since the RNA granule is in itself membraneless, this is a truly membrane-free axonal transport complex wherein the GAR domain provides an essential and direct link between nucleolin containing RNA granules and the anterograde transport machinery. There is *in vitro* evidence for other membrane-free RBP-kinesin complexes (Baumann *et al*, 2020; Wu *et al*, 2020). Thus, mRNA transport to cellular extremities can be conducted by diverse carriers utilizing both membrane-associated and membrane-free transport complexes. *In vivo* evidence is therefore required to determine which of these mechanisms is physiologically important. Our gene editing approach provides such evidence for GAR-mediated transport of nucleolin complexes, clearly identifying *Kpnb1*, *mTOR*, and *Inpp5f* mRNAs as being critically dependent on this specific transport complex for localization to sensory axons both in culture and *in vivo*. Our pulldowns and RNA-seq analyses have identified a host of additional mRNAs that are likely co-transported in the same complex, and complex stoichiometry and dynamics will be an intriguing topic for further investigation.

Generation of GAR mutant mice, albeit limited to heterozygotes, also allowed evaluation of physiological consequences of disruption of nucleolin complex transport to axons. Our previous work had proposed a size sensing mechanism dependent on microtubule

motor-based localization of RNA encoding importin β1 and mTOR, coupled with regulated local protein synthesis, to enable cytoskeleton length sensing for cell growth regulation (Rishal & Fainzilber, 2019). The model predicts that perturbation or reduction of the complex in the axon should lead to accelerated axonal growth, as previously shown by knockdown of molecular motors (Rishal *et al*, 2012), 3′UTR deletion in *Kpnb1* (importin β1) mRNA (Perry *et al*, 2016), and AS1411 perturbation of kinesin–nucleolin interactions (Perry *et al*, 2016). We have now shown that $GAR^{+/-}$ neurons also reveal accelerated axon growth, providing independent support for this growth control mechanism in a genetically engineered mouse model. Moreover, identification of Inpp5f, a known cell size regulator (Zhu *et al*, 2009; Zou *et al*, 2015), as an additional component of the RNA ensemble transported by the complex is an intriguing lead for future research.

We have shown that the diverse subcellular localizations of nucleolin are largely determined by its single small GAR domain, acting via multiple mechanisms—LLPS, protein–protein interaction, and protein–membrane association. This versatility suggests that different regulatory mechanisms must exist to allow the GAR domain to discriminate or translocate between these different options. Elucidating such regulation will be of great interest for the future, and one promising possibility is the activity of protein arginine methyltransferases (PRMTs). PRMT methylation of arginines has been described in a spectrum of fundamental cellular processes, including RNA processing, nucleocytoplasmic distribution, signal transduction, and LLPS (Guccione & Richard, 2019; Tsang *et al*, 2019). A brain-enriched membrane-attached PRMT has been described (Lee *et al*, 2005; Park *et al*, 2019), and thus, it is intriguing to speculate that arginine methylation may be involved in translocation of GAR interactions between motors and membranes. Alternatively, local translation of nucleolin cargo mRNAs may generate local modifications of the cellular milieu that affect interactions of the GAR domain. For example, Inpp5f/Sac2 regulates phosphoinositides in the endocytic recycling pathway (Hsu *et al*, 2015), so its local translation in a restricted axonal subdomain might well change local membrane characteristics to modulate GAR association.

Finally, many axonal RBPs harbor a GAR domain and a number of known neurodegeneration-associated mutations in RBPs are found in their GAR domains. For example, mutations in the GAR domains of FUS, EWSR1, and TAF15 are associated with amyotrophic lateral sclerosis (Kapeli *et al*, 2017), and methylation or citrullination within GAR domains affects FUS aggregation and activity (Hofweber *et al*, 2018; Tanikawa *et al*, 2018). The multiple roles of the GAR domain as a key localization determinant for nucleolin may be mirrored in many other RBPs, with implications for their cellular functions and for understanding the consequences of disease-associated mutations therein.

Materials and Methods

Mice

All animal experiments were reviewed and approved by the Institutional Animal Care and Use Committee at the Weizmann Institute of Science or the University of South Carolina. Adult C57BL6/OlaHSD and BALB/c mice were purchased from Harlan Laboratories (Envigo, Israel), and male Sprague Dawley rats (175–250 g) were purchased from Charles Rivers Laboratories. The C57BL/6YFP16 mice (Feng *et al*, 2000) were maintained at the Veterinary Resources of the Weizmann Institute. Nucleolin $GAR^{+/-}$ were generated and bred by the Weizmann Institute Veterinary Resources Department's core facility for transgenics and knockouts as described in the detailed Methods section. All animals were housed in the Veterinary Resources Department of the Weizmann Institute or Animal Resource Facility of the University of South Carolina in a temperature-controlled room under a 12-h light/dark cycle. Water and food were available *ad libitum*. Both female and male mice were used alternately in all experiments. Per biological replicate, mice for all conditions were sex and age matched, and littermates were used whenever possible. Tissue was extracted from animals 8–20 weeks of age.

Primary neuronal cultures

Dorsal root ganglia (DRG) from 8- to 12-week-old mice were dissected and dissociated for neuron cultures with 100 U of papain (P4762, Sigma) followed by treatment with 1 mg/ml collagenase-II (11179179001, Roche) and 1.2 mg/ml dispase-II (04942078001, Roche) for additional 25–30 min. The ganglia were mechanically triturated in HBSS supplemented with 10 mM glucose, and 5 mM HEPES (pH 7.35), by aspiration in a glass Pasteur pipette whose opening was narrowed by fire polishing and was pre-covered in serum-containing media. Cells were then laid on a 20% Percoll cushion in Leibovitz L15 medium and recovered through centrifugation at 1,000 *g* for 8 min. Cells were washed briefly in growth medium and plated on pre-coated glass coverslips or plates in growth medium (F12 supplemented with 10% fetal bovine serum and antibiotic formulation Primocin (InvivoGen) according to manufacturer's instructions). Pre-coating included a first step of coating with poly-L-lysine (P4832, Sigma) followed by laminin (23017-015, Invitrogen). When cells were grown for > 2 days, growth media was supplemented with 10 μM cytosine β-D-arabinofuranoside (AraC) starting at 24 h after plating and replenished every 48 h. For compartmentalized cultures (modified Boyden chambers), cells were plated on Millicell 1-μm pore size inserts (MCRP06H48, Millipore) as previously described (Willis & Twiss, 2011) and allowed to grow for 3 days prior to extraction. Where indicated, cells were treated with 10 μM AS1411 (GGTGGTGGTGG TTGTGGTGGTGGTGG) or 10 μM control DNA (CCTCCTCCTCCTT CTCCTCCTCCTCC) oligonucleotides (Integrated DNA Technologies) as described before (Perry *et al*, 2016). All cells were incubated at 37°C and 5% CO_2. For rescue experiments as shown in Figs 7, EV4, and EV5, DRGs isolated from rats were transfected with HA-Dendra2-nucleolin-WT or HA-Dendra2-nucleolin-DGAR constructs (without the 3′UTR of Ncl) using Amaxa Nucleofector after dissociation. Neurons were cultured and 3 h later transfected with 50 nM control siRNAs (Sahoo *et al*, 2020) or two siRNAs targeting 3′ UTR of *Ncl* mRNA (siRNA 1: GUUGAAUGACAGAG CCUUUUU; siRNA 2: GGACAUUCCAAGACAGUAAUU) using DharmaFECT-3. Cultures were fixed 96 h later, and FISH/IF was performed. RT-ddPCR and immunoblotting for Ncl mRNA and protein, respectively, were performed on sister cultures to validate knockdown of endogenous mRNA.

Cell lines

HEK-293 (human, female, RRID: CVCL_0045), U937 (human, male, RRID: CVCL_0007) and Neuro-2A (mouse, male, RRID: CVCL_0470) cells were purchased from ATCC (Cat# CRL-1573, CRL-1593, CCL-131, respectively). HEK-293 and Neuro-2A cells were cultured in DMEM (Gibco), supplemented with 10% fetal bovine serum (Gibco), 100 U/ml *penicillin,* and 100 μg/ml streptomycin. U937 cells were grown in RPMI-1640 medium (Biological Industries) supplemented with 10% fetal bovine serum (Gibco), 100 U/ml *penicillin,* and 100 μg/ml streptomycin. All cells were incubated at 37°C (Farin *et al*, 2011) and 5% CO_2. The cell lines used were not authenticated.

Plasmids and transfections

Full-length mouse nucleolin ORF was subcloned into a pcDNA3.1-based mammalian expression vector from a plasmid kindly provided by Ronit Pinkas-Kramarski (Farin *et al*, 2011). The sequence was modified using restriction-free cloning to generate GAR deletion (amino acids 646-697 from UniProt sequence P09405) and GAR(N) variants, and to introduce N-terminal HA-Dendra2 tags, as well as generating a construct expressing HA-Dendra2 alone. Phusion polymerase (Thermo Fisher) was used for mutagenesis, according to manufacturer's instructions. Dendra2 sequence was cloned from pDendra2 construct (Evrogen). For AAV generation, HA-Dendra2 fusions with full-length nucleolin, nucleolin with deleted GAR deletion, and domain were subcloned under the human synapsin (hSynI) promoter in a previously described AAV genomic vector (Mahn *et al*, 2018; Marvaldi *et al*, 2020), using PCR with primers tailed with AscI and EcoRV restriction sites. Kif5a expression plasmid was obtained from Addgene (#31607). HEK-293 and N2a cells were purchased from ATCC (CCL-131) and cultured in DMEM (Gibco), supplemented with 10% fetal bovine serum (Gibco), 100 U/ml *penicillin,* and 100 μg/ml streptomycin. U937 cells were purchased from ATCC (CRL-1593.2) and grown in RPMI-1640 medium (Biological Industries) supplemented with 10% fetal bovine serum (Gibco), 100 U/ml *penicillin,* and 100 μg/ml streptomycin. For transfection of HEK-293 cells, jetPEI (Polyplus-transfection) was used according to manufacturer's instructions. In experiments where HA-Dendra2-nucleolin or HA-Dendra2 constructs were cotransfected with Kif5a, a 4:1 expression ratio was used to compensate for differences in expression levels.

Antibodies

Following primary antibodies were used for this study: rabbit anti-nucleolin (Abcam, ab50279, 1:1,000 for WB), rabbit anti-nucleolin (ProteinTech, 10556-1-AP, 1:100 for IF), rabbit anti-Kif5a (Abcam, ab5628, 1:1,000 for WB, 1:100 for Wes), rabbit anti-HA (Sigma, H6908, 1:1,000 for WB), rabbit anti-LAMP1 (Abcam, ab24170, 1:1,000 for WB), mouse anti-GAPDH (Millipore, MAB374, 1:5,000 for WB), mouse anti-β-III tubulin (R&D systems, MAB1195, 1:1,000 for WB), mouse β-III tubulin (Tuj1) (BioLegend 801202, 1:500 for IF), mouse anti-NFH (Developmental Studies Hybridoma Bank, RT97, 1:200 for IF), chicken anti-NFH (Abcam, ab72996, 1:1,000 for IF), mouse anti-neurofilament (BioLegend 837904, 1:1,000 for IF), and sheep anti-digoxigenin (Roche, 11207733910, 1:2,000 for ELISA). HRP-conjugated secondary antibodies for immunoblots were purchased from Bio-Rad Laboratories, Alexa Fluor Secondary antibodies were purchased from Jackson ImmunoResearch, and streptavidin-HRP was purchased from Abcam (ab7403, 1:10,000).

ELISA assay for AS1411-binding peptides

Streptavidin-coated 96-well ELISA plates (R&D systems, CP004) were washed twice in PBS-T (PBS 1× + 0.05% Tween-20), then incubated for 1 h at room temperature with 0.025 μM Biotinylated peptides, blocked by incubation with 1% BSA (Sigma, A9647) in PBS for 30 min at 37°C, and then incubated with 0.04 μM digoxigenin (3′-DIG) AS1411 or control aptamer (Integrated DNA Technologies) in PBS for 1 h at room temperature. Then, plates were incubated with HRP-conjugated anti-DIG antibody (Roche, 11207733910) diluted 1/2,000 in 1% BSA-PBS for 30 min at 37°C. Signal was detected using TMB ELISA substrate (Sigma, T0440). Plates were washed three times before each subsequent step with PBS-T and five times prior to signal detection. Signal was read using a Tecan5 plate reader reading absorbance at 360 nm wavelength.

Axoplasm isolation

Mouse sciatic nerve axoplasm was isolated as previously described (Rishal *et al*, 2012). In brief, freshly dissected sciatic nerves were collected in Nuclear Transport buffer (TB) at a ratio of 1 SN/50 μl buffer (20 mM HEPES, 110 mM KAc, 5 mM MgAc, pH 7.4 supplemented with Complete protease inhibitor EDTA free (Roche 1187358000), phosphatase inhibitor cocktail 2 (1/1,000, Sigma 5726), phosphatase inhibitor cocktail 3 (1/1,000, Sigma P0044), and RNAse inhibitors (200 U/ml, RNAseIn, Promega N251B). Tissue was manually ground with a micropestle in a microtube until it lost its fibrous consistency. Lysates were centrifuged 10,000 *g* for 10 min at 4°C, and pellet was discarded.

Immunoprecipitation

Nucleolin immunoprecipitation from axoplasm was conducted as follows: Approximately 200 μg of axoplasm/protein lysates were incubated with 10 μg antibody for 3 h, then supplemented with 100 μl Protein G magnetic beads (Dynabeads, Thermo Fisher Scientific 10004D), and pre-blocked with salmon sperm DNA (10 μl DNA per 100 μl beads for 1 h 4°C), for additional 1 h. Incubation buffer was adjusted to final 0.1% NP-40 to avoid bead aggregation. All incubation steps were done at 4°C with overhead rotation. Beads were washed with increasing NP-40 concentration as follows: TB-0.1% NP-40 for 3–5 min, TB-0.5% NP-40 3–5 min, TB-1% NP-40 1 min, TB-no detergent 3–5 min, then transferred to a clean Eppendorf tube in TB without detergent. Elution from beads was conducted by denaturing the proteins from the beads with Laemmli sample buffer or WES sample buffer supplemented with DTT to a final concentration of 40 mM for 5 min at 95°C.

Axoplasm pulldown with biotinylated peptides

Axoplasm lysates were incubated overnight at 4°C with streptavidin magnetic beads (Dynabeads M-280, Thermo Fisher Scientific 11205D) preconjugated to biotinylated peptides by incubation with 2 μM peptides in PBS-T for 1 h at room temperature. A pre-cleaning

step was added, clearing the sample with beads preconjugated to control peptide (A3 or N4) for 3 h at 4°C prior to the overnight incubation with target or control peptides. Washes were as indicated for immunoprecipitation, followed by 2 washes with mass spectrometry grade water (Fluka analytical 39253) to remove any traces of detergents and salts.

Mass-spectrometric analysis

Sample-incubated streptavidin magnetic beads were resuspended in 20 µl 5 mM DTT 100 mM NH_4HCO_3 and incubated for 30 min at room temperature. After this, iodoacetamide was added to a final concentration of 7.5 mM, and samples incubated for 30 additional minutes. 0.5 µg of sequencing grade trypsin (Promega) was added to each sample and incubated at 37°C overnight. Supernatants of the beads were recovered, and beads digested again using 0.5 µg trypsin in 10 µl 100 mM NH_4HCO_3 for 2 h. Peptides from both consecutive digestions were combined and recovered by solid-phase extraction using C18 ZipTips (Millipore), eluted in 15 µl 50% acetonitrile 0.1% formic acid, and resuspended in 5 µl 0.1% formic acid for analysis by LC-MS/MS. Peptides resulting from trypsinization were analyzed on a QExactive Plus (Thermo Scientific), connected to a NanoAcquity™ Ultra Performance UPLC system (Waters). A 15-cm EasySpray C18 column (Thermo Scientific) was used to resolve peptides (90-min 2–30% gradient with 0.1% formic acid in water as mobile phase A and 0.1% formic acid in acetonitrile as mobile phase B). MS was operated in data-dependent mode to automatically switch between MS and MS/MS. The top 10 precursor ions with a charge state of 2+ or higher were fragmented by HCD. Peak lists were generated using PAVA in-house software (Guan *et al*, 2011). All generated peak lists were searched against the mouse subset of the UniProtKB database (UniProtKB.2013.6.17) (plus the corresponding randomized sequences to calculate FRD on the searches), using Protein Prospector (Clauser *et al*, 1999). The database search was performed with the following parameters: a mass tolerance of 20 ppm for precursor masses; 30 ppm for MS/MS, cysteine carbamidomethylation as a fixed modification and acetylation of the N terminus of the protein, pyroglutamate formation from N-terminal glutamine, and oxidation of methionine as variable modifications. All spectra identified as matches to peptides of a given protein were reported, and the number of spectra (Peptide Spectral Matches, PSMs) used for label-free quantitation of protein abundance in the samples.

Western blot and Wes capillary immunoanalysis

For Western blot, proteins were blotted on nitrocellulose membranes using a Trans-Blot Turbo™ Transfer System (Bio-Rad). Membranes were blocked with 5% nonfat dry milk in TBST buffer for 1 h. Primary antibodies were incubated for 1 h at room temperature or overnight at 4°C with shaking. Secondary HRP-conjugated antibodies were diluted 1:10,000 in TBST and incubated for 1 h at room temperature. Blots were developed using Radiance ECL substrate (Azure Biosystems) or SuperSignal™ West Femto (Thermo Fisher Scientific) or Clarity western ECL (Bio-Rad) substrates on an Amersham Imager 680 or Bio-Rad ChemiDoc. Automated capillary electrophoresis immuno-quantification runs were conducted on a WES instrument (ProteinSimple) according to manufacturer recommendations. The indicated MW are determined based on an internal standard of known MW spiked in to every capillary.

Surface plasmon resonance analysis

KLC binding to R4 GAR and N4 GAR-derived peptides was monitored by surface plasmon resonance (SPR) on a Biacore S200 system using a biotinylated streptavidin chip (Series S SA). Recombinant KLC2 was injected with different concentrations (5–160 nM) in a single cycle kinetic mode on biotinylated R4 or N4 GAR-derived peptides, or free biotin. Before data collection, a normalization cycle followed by a priming cycle was run to stabilize the instrument. Binding assays were performed in triplicates in PBS-T buffer with a flow rate of 30 µl/min at 25°C. 120-s contact time was required to achieve steady-state binding, and regeneration of the chip surface was achieved by a 30-s injection of 2 mM NaOH in water. The dissociation equilibrium constant, KD, was determined by fitting the sensogram to a build in global fitting routine, using a 1:1 model using S200 Evaluation Software 1.1.

Molecular simulations of peptide-phospholipid bilayer interactions

Simulations in Fig 3A. In two separate simulation setups, three previously equilibrated peptides of each sequence (R4, N4, and K4) were placed either freely in a box with only water (500 ns for each sequence) or in a box with water and membrane composed of phosphatidylcholine and phosphatidylserine (PC:PS, 4:1) (500 ns for each sequence + 3 additional independent runs, each 50 ns long). Both systems contained 150 mM KCl including additional K^+ ions to neutralize the negative charge of peptides (in case of R4 and K4). All MD simulations were performed using the Gromacs 5.1.2 package (Abraham *et al*, 2015). Calculations were done with charmm36 force field (Klauda *et al*, 2010), and the membrane was prepared and solvated using Charmm-gui interface by employing the CHARMM-GUI server (Wu *et al*, 2014). The peptides were built in VMD (Humphrey *et al*, 1996) using its Protein builder tool.

Simulations in Appendix Fig S3. Newton's equations of motion were integrated by employing the leap-frog algorithm (Hockney *et al*, 1974) with a time step of 2 fs. The trajectory frames were recorded every 10 ps and energy every 2 ps. For simulations with a membrane, energy was recorded every 2 ps. A cutoff of 1.2 nm was applied to short-range electrostatic interactions while long-range electrostatics was calculated with the use of the particle mesh Ewald method (Darden *et al*, 1993). Van der Waals interactions were truncated at 1.2 nm; in addition, for the membrane simulations, the van der Waals potentials were decreased using Force-switch so that the forces went smoothly to zero between 1.0 and 1.2 nm. Bonds with hydrogen atoms, and all bonds for membrane setup, were constrained by the LINCS algorithm (Hess *et al*, 1997), and water molecules were kept rigid by the SETTLE algorithm (Miyamoto & Kollman, 1992). The temperature of the system was maintained at 310 K using the velocity rescaling thermostat with a stochastic term, and the Parrinello–Rahman barostat was utilized for isotropic, resp. semi-isotropic for membrane simulations, pressure coupling with a reference pressure of 1.01 bar. The time constants of the thermostat and barostat were 0.5 and 10 ps, respectively, and 1 and 5 ps for the membrane setup. The peptides were built in VMD Protein

builder. Each structure was then equilibrated and minimized, and in order to provide enough time for the peptides to accommodate, a 100-ns long simulation was run. The simulation box was 6 × 6×6 nm big containing ~7,000 water molecules together with 150 mM KCl including additional K^+ ions to neutralize the negative charge of peptides (in case of R4 and K4). In the case of simulations of peptide's triplets, box 7 × 7×7 nm containing ~11,000 water and the same ionic strength strategy was used. Peptides were placed in the box randomly in a distance where they did not initially interact with each other. In all simulations, water molecules were described by the TIP3P water model (Jorgensen *et al*, 1983), and to account for electric polarizability, all charges of K^+ and Cl^- ions were rescaled by a factor of 0.75 (Leontyev & Stuchebrukhov, 2011). The membrane was prepared and solvated using Charmm-gui interface by employing the CHARMM-GUI server. The bilayer was equilibrated and minimized following the standard minimization and equilibration protocol provided by CHARMM-GUI. The simulation box of size 8 × 8×14 nm contained a PC:PS (4:1) bilayer consisting of 160 PC lipids and 40 PS lipids, 150 mM KCl, including additional K^+ ions to neutralize the negative charge of the membrane and peptides (in case of R4 and K4) and ~21,000 water molecules. Peptides were placed in the box randomly (and it was checked that it does not depend on orientation or the initial distance of peptides from the membrane, see Fig 3A) in a distance where they did not initially interact with membrane leaflets or with each other. The simulations were performed with three peptides to be able to observe pair or cluster formation but at the same time to keep the simulations feasible and not costly. To ensure that our 500-ns long simulations are converged, the analysis was processed separately for the first 250 ns and the last 250 ns and the results were compared. There are no differences between the two analyses which means the simulation is converged. Also, to be sure that the initial distribution of peptides in boxes does not affect the result, another three short 50-ns simulations for each N4, R4, and K4 sequence were performed yielding similar results.

Cellular peptide uptake assays

DRG neurons expressing YFP under the Thy1 promoter (Feng *et al*, 2000) were cultured on a 4 Well Glass-Bottom slide chamber (μ-Slide, ibidi 80427) for 24 h prior to treatment. For cold treatment (4°C), plates were taken out of the incubator and onto ice and taken in to the cold room (2-8°C) to cool for 20 min. Then, medium was replaced with cold (4°C) growth medium supplemented with 5 μM R4 (FGGRGRGGFGGRGGFRGG) or N4 (FGGNGNGGFGGNGGFNGG) peptides N-terminally conjugated with TAMRA (Sigma). Following additional 30 min, cells were washed three times in cold PBS, fixed in cold 4% PFA for 20 min, and imaged in PBS using Olympus FV1000 Confocal laser-scanning microscope with a 60× water immersion objective (UPLSAPO 60× O NA:1.35). Average TAMRA intensity per pixel was measured using FIJI software. Cells were traced manually based on the phase contrast channel.

For analysis of peptide uptake into HEK-293 and U937 cells, 5 μM TAMRA-conjugated peptides were added to the growth medium for 60 min. Then, cells were collected into 15-ml tubes for washing with cold PBS in pre-cooled centrifugation (2 × 2 min, 1,000 × *g*). Cells then were suspended in 400 μl cold PBS and filtered through a nylon mesh into 5-ml tube to obtain a uniform single-cell suspension. Cells were analyzed on a FACS-LSRII cytometer (BD Biosciences) using BD FACSDIVA software (BD Biosciences).

Cell surface biotinylation

On the day following transfection, HEK-293 cells grown on 10-cm plates (one plate per sample) were washed twice with ice-cold PBS and treated with 0.5 mM sulfo-NHS-SS-biotin (Thermo Scientific 21331) in PBS for 30 min at 4°C with gentle rocking. Free sulfo-NHS-SS-biotin was removed, and unreacted reagent was quenched by adding ice-cold 50 mM Tris–HCl in PBS pH 7.4. Cells were washed once with PBS and once with PBS + 0.1 mM oxidized glutathione (Sigma G4376). Proteins were extracted 30 min lysis in RIPA buffer (50 mM Tris–HCl, pH 8.0, 150 mM NaCl, 1% NP-40, 0.5% sodium deoxycholate, 0.1% SDS) supplemented with Complete EDTA-free protease inhibitor cocktail (Roche 1187358000) and 0.1 mM oxidized glutathione. Lysates were centrifuged for 12,000 *g* to pellet debris, and 1/20 of lysates was used for input samples. The remainder of the lysate was used for pulldown of biotinylated proteins with 30 μl of MyOne Streptavidin C1 Dynabeads (Thermo Scientific 65002) for 1 h on a rotator at 4°C. Beads were washed for 4 × 5 min at 4°C and biotinylated peptides eluted by incubating with 50 mM DTT in PBS for 30 min at 50°C. Efficiency of cell surface labeling was assessed by Western blotting input samples with streptavidin-HRP.

Generation of AAV-PHP.S vectors and transduction of cultured DRG neurons

ORFs of HA-tagged nucleolin full-length, nucleolin ΔGAR, nucleolin GAR(N), and nucleolin-derived GAR domain were subcloned into an AAV plasmid under the human Synapsin I (hSynI) promoter to ensure neuronal specificity (Mahn *et al*, 2018; Marvaldi *et al*, 2020). For AAV production, we used AAVpro HEK-293T cells and (Takara Bio 632273) AAVpro® Purification Kit for All Serotypes from Takara Bio (#6666) according to manufacturer's instructions. Four 15-cm plates were transfected with 20 μg of DNA (AAV plasmid containing the expression cassette, pAAV-PHP.S (Addgene # 103006), and pAdDeltaF6 (University of Pennsylvania Vector Core) helper plasmids) in equimolar ratios using jetPEI® (Polyplus) in DMEM medium without serum or antibiotics. Medium (DMEM, 20% FBS, 1 mM sodium pyruvate, 100 U/ml penicillin, and 100 mg/ml streptomycin) was added on the following day to a final concentration of 10% FBS, and virus particles were harvested 3 days after transfection. Virus titers (as determined by RT–qPCR) were in the range of 10^{12}–10^{13} viral genomes/ml. For infection of cultured neurons, cells were transduced with the viral stock at a 1:200 dilution simultaneously with seeding. The cells were replated on glass-bottom 35-mm MatTek dish for hypoosmotic treatment experiment or coverslips for evaluation of neurite outgrowth 8–9 days after transduction. Aforementioned experiments were conducted on the next day after replating.

Hypoosmotic treatment of cultured cells

Adult mouse DRG neurons transduced with AAV-PHP.S (Chan *et al*, 2017) encoding HA-Dendra2-nucleolin (full length and ΔGAR), or N2a or HEK-293 cells transfected with HA-Dendra2-nucleolin (full length and ΔGAR) expression plasmids were live imaged with the Nikon Ti-LAPP illumination system equipped with a temperature-

controlled chamber and an Andor EMCCD camera. Cells were incubated with 10 μM Hoechst 33342 in medium for 10 min prior acquisition. Images were acquired in DAPI, GFP, TRITC, and DIC channels at ×60 magnification with Nikon CFI plan apochromat 60× oil lambda objective. Medium was removed, and the cells were immediately refocused and imaged or the $t = 0$ image, followed by careful addition of 1 ml ddH2O by pipetting and image acquisition using a same setting with 42 s interval for 5 min. Images were analyzed by NIS-Elements software (Nikon).

Generation of nucleolin GAR knockout mice using CRISPR-Cas9

GAR knockout lines were generated by using two sgRNAs to create a deletion in the nucleolin coding sequence. The sgRNAs were designed to minimize off target deletions in non-specific areas in the genome and to maximize the probability of Cas9 cleavages at the targeted sites, using CHOPCHOP (v.2, chopchop.cbu.uib.no) and other tools detailed in the Benchling implementations (www.benchling.com), see also Appendix Table S3. Guides were designed to cut in exon 13 and exon 14, flanking all RGG repeats in the GAR domain. Selected sgRNAs were prepared in-house as previously described (Ran *et al*, 2013). In brief, sgRNA were cloned into px459 plasmid. T7 promotor sequence was fused to sgRNA target sequence by PCR reaction, and sgRNAs were *in vitro* transcribed with MEGAshortscript (Ambion cat. AM1354) and cleaned with MEGAclear kit (Ambion cat. AM1908). sgRNA ability to direct Cas9 recombinant protein to the appropriate DNA sites was tested *in vitro* using Guide-it sgRNA Screening Kit (Clontech Cat. No. 631440) with PCR product containing the relevant part of the gene (940 base pairs) amplified from genomic DNA as template (primers: Fwd-GCATGGAGAACTTGGGTCTG, Rev-ATGAAGCTGTTCCCCACCAAT). Cas9 mRNA was *in vitro* transcribed with mMESSAGE mMACHINE T7 Ultra Kit (Ambion cat. AM1345) from a linearized plasmid and cleaned with MEGAclear kit (Ambion cat. AM1908). Genome edited animals were generated by the Weizmann Institute Transgenic Unit by microinjection. Cas9 mRNA and the two sgRNAs (sgRNAa: GGCUUCCGAGGCGGCAGAGGAGG, cuts at position 666 of NM_010880.3 (Refseq sequence), end of GAR; sgRNAb;GAAGGUGGCUUUGGUGGUCGAGG, cuts at position 898 of Refseq sequence, beginning of GAR) were microinjected into fertilized oocytes from superovulated CB6 F1 donor mice. Founders were crossed with WT C57BL/6J-OlaHsd for multiple generations. Genotyping was done by PCR on genomic DNA extracted from 3 to 4 weeks' pups' tails, using the screening primers indicated above. For each sgRNA, potential genomic alterations in off-targets within genes were further screened by PCR on DNA from tails of F3 progeny of the founder further bred for experiments (Appendix Table S3 for primer sequences).

Fluorescent *in situ* hybridization

For FISH in *in vitro* cultured neurons, DRG neurons were isolated from adult rats aged 2-3 months and cultured as described previously (Twiss *et al*, 2000). Briefly, DRG neurons were harvested in Hibernate-A medium (BrainBits) and then dissociated as described. After centrifugation and washing in DMEM/F12 (Life Technologies), cells were resuspended in growth medium consisting of DMEM/F12, 1 × N1 supplement (Sigma), 10% fetal bovine serum (HyClone), and 10 μM cytosine arabinoside (Sigma). Dissociated DRGs were plated immediately on laminin/poly-L-lysine-coated coverslips in growth media containing 10 μM of control or AS1411 aptamer. DRG neurons were let to grow for 48 h followed by replating and letting the cells grow for next 18 h. Further DRG cultures were fixed for 15 min in 2% PFA in PBS and then processed for FISH as described (Sahoo *et al*, 2018). RNA-FISH was performed using custom 5′ Quasar 670-labeled "Stellaris" probes against rat *Inpp5f* mRNA (Biosearch Technologies, Cat# SS561665-01-48), 5′ Quasar 570-labeled "Stellaris" probes against rat *mTor* mRNA (Terenzio *et al*, 2018), and 5′ Quasar 570-labeled "Stellaris" probes against rat *Kpnb1* mRNA (Perry *et al*, 2016). 5′ Quasar 570- or Quasar 670-labeled scrambled probes were used as controls for specificity; samples processed without addition of primary antibody were used as control for antibody specificity. Primary antibody consisted of RT97 mouse anti-NF (1:200). FITC-conjugated donkey anti-mouse (1:200) was used as secondary. Samples were mounted as above and analyzed using a Leica DMI6000 epifluorescent microscope with ORCA Flash ER CCD camera (Hamamatsu).

For FISH in tissue sections, sciatic nerves from wild-type and nucleolin $GAR^{+/-}$ mice were dissected from adult mice aged 8–10 weeks (both sexes were used) and fixed for 4 h at room temperature in 2% paraformaldehyde in PBS, washed 3 × 5 min with PBS, and cryoprotected overnight in in 30% buffered sucrose at 4°C. Custom-designed Quasar 570-labeled Stellaris probes (Bioresearch Technologies) were used to detect *mTor* and *Kpnb1* mRNA in sciatic nerve axons from wild-type or $GAR^{+/-}$ mice. FISH was performed on 10-μm-thick sciatic nerve sections as previously described (Terenzio *et al*, 2018) with some modifications. Briefly, tissue sections were washed three times in 20 mM glycine (in 1× PBS) for 5 min each followed by three 5 min washes in 0.25 M $NaBH_4$ (in 1X PBS). This was followed by a quick wash in 0.1 M triethanolamine then a 10 min wash in 0.1 M triethanolamine + 0.25% acetic anhydride. After a quick wash in 2× SSC, tissue sections were dehydrated in a series of increasing concentrations of ethanol for 3 min each (70–95, to 100%) followed by delipidation in chloroform for 5 min. After delipidation, tissue sections were immediately put in 100% ethanol and then 95% ethanol for 3 min each. After two washes in 2X SSC, tissues were incubated in 0.2 M HCl for 10 min. Tissue sections were permeabilized in 1% Triton X-100 in PBS for 2 min and then washed three times in PBS. Sections were then equilibrated in 2X SSC supplemented with 10% formamide. Sections were incubated with Stellaris probes (0.25 μM), mouse SMI-312 anti-phospho-NF (1:1,000; BioLegend 837904), Tuj1 (1:500; BioLegend 801202), and mouse RT97 (1:200; DHSB) overnight at 37°C in a humidified chamber. After hybridization, sections were washed twice for 30 min each time in 2X SSC supplemented with 10% formamide followed by three washes in 2X SSC. Sections were washed with 0.3% Triton X-100 in 1× PBS then incubated in donkey anti-mouse FITC secondary antibody (1:200; Jackson Immuno-Res) in 0.3% Triton X-100 in PBS with 10X blocking buffer (1:100; Roche) for 1 h at room temperature. Sections were then washed three times for 5 min each time in PBS, rinsed in DEPC water, and then coverslipped with Prolong Gold Antifade with DAPI (Invitrogen).

Immunofluorescence analysis

Tissue sections were washed in 20 mM glycine in PBS three times 10 min each time, washed in 0.25 M $NaBH_4$ three times 5 min each

time, and then permeabilized in 0.2% Triton X-100 in PBS. After three rinses in PBS, tissue sections were blocked in blocking buffer (10% donkey serum, 0.1% Tween-20, 20 mM glycine, PBS). Sections were incubated in rabbit nucleolin, mouse SMI-312, mouse Tuj1, and mouse RT97 primary antibodies overnight at 4°C. After three 5 min washes in PBS, sections were incubated in donkey anti-rabbit Cy5 and anti-mouse FITC secondary antibodies (1:200 each; Jackson Immuno-Res) for 1 h at room temperature. After three 5 min washes in PBS, sections were rinsed in ddH_2O then cover-slipped with Prolong Gold Antifade with DAPI.

Dendra conversion time-lapse imaging

Adult mouse DRG neurons transfected by Amaxa Nucleofector II with HA-Dendra2-GAR(WT) or with HA-Dendra2-GAR(N) expression plasmids were live imaged with the Nikon Ti-LAPP illumination system equipped with a temperature-controlled chamber, Digital Mirror Device (DMD), and an Andor EMCCD camera. Cells were grown 48 h in complete F12 medium prior acquisition. Images were acquired in GFP, TRITC, and DIC channels at ×60 magnification with Nikon CFI plan apochromat 60× oil lambda objective. The photoconversion was performed in the cell body area by DAPI channel (50% of maximum led intensity for 20 s) using DMD module. The images were collected using GFP and TRITC channels at 10-s interval for 20 min. DIC channel was used prior to photoconversion and in last four time points. Images were analyzed by NIS-Elements software (Nikon). A neurite segment located at a distance of 60–90 μm from the cell body was selected for the kinetic intensity analysis.

Image analysis

FISH/IF images were captured using a Leica SP8X confocal microscope with HyD detectors. For nucleolin IF, Leica SP8X with Lightning detection was used to capture images. Scrambled probes were used to set the image acquisition parameters to limit acquiring non-specific signals. For IF, the no primary antibody control was used to set the image acquisition parameters. For each nerve, xyz scans of three randomly chosen regions of interest (123.29 × 123.29 μm) with a z depth of 4.5 μm (15 optical planes) were scanned with a 63× oil immersion objective (1.4 NA). The colocalization plug-in in ImageJ (https://imagej.nih.gov/ij/plugins/colocalization.html) was used to extract the mRNA or protein signal in each optical plane that overlapped with axonal markers (NF and Tuj1). The axon-only mean intensity values were normalized to the NF and Tuj1 signals in each XY plane. For analysis, the values of each optical plane were averaged for each ROI. The lowest and highest value for each animal (n = 4 or 5) was discarded. The average axon-only scramble signal were subtracted from the axon-only mRNA signals from each ROI average.

RNA-seq analysis

RNA sequencing libraries were prepared using the SMARTSq v4 RNA Ultra Low Input (10 pg) + Nextera XT library kit. Libraries were indexed and sequenced by HiSeq4000 with 50 bp paired-end reads, and at least 41 M reads were obtained for each sample. Quality control was performed on base qualities and nucleotide composition of sequences, mismatch rate, mapping rate to the whole genome, repeats, chromosomes, key transcriptomic regions (exons, introns, UTRs, genes), insert sizes, AT/GC dropout, transcript coverage, and GC bias to identify problems in library preparation or sequencing. Reads were aligned to the mouse mm10 reference genome (GRCm38.75) using the STAR spliced read aligner (ver. 2.4.0). Average input read counts were 66.0 M, and average percentage of uniquely aligned reads were 72.6%. Total counts of read fragments aligned to known gene regions within the mouse (mm10) ensembl (GRCm38.80) transcript reference annotation are used as the basis for quantification of gene expression. Fragment counts were derived using HTSeq program (ver. 0.6.0). Genes with minimum of 5 counts for at least one condition (all replicates) were selected, and differentially expressed transcripts were determined by Bioconductor package EdgeR (ver. 3.14.0). Scripts used in the RNA sequencing analyses are available at https://github.com/icnn/RNAseq-PIPELINE.git. The Rank-Rank Hypergeometric Overlap (RRHO) algorithm (Plaisier *et al*, 2010) was used to determine the overlap between transcripts enriched in the nucleolin IP dataset, and transcripts depleted in the $GAR^{+/-}$ axons, as compared to their WT counterparts. Transcripts were sorted by directional *P*-values, followed by RRHO with a sliding window of 50. The overlap transcript lists were obtained for the lowest adjusted *P*-values. The resulting overlap transcript list was further filtered using a threshold of fold change > 2 in IP over control, for both Ncl and Kif5a IPs, yielding a list of 488 mutually enriched in Ncl and Kif5a IPs and downregulated in $GAR^{+/-}$ versus WT dataset. These 488 transcripts were clustered using the "hclust" function in R, using the Pearson method. Enrichment analysis was done on overlapping and unique gene lists using Ingenuity Pathway Analysis (IPA, version 42012434, QIAGEN).

RT–qPCR and RT-ddPCR analyses

For RT–qPCR RNA was extracted from DRG neurons cultured in Boyden chambers as previously described (Willis & Twiss, 2011). cDNA was prepared from 500 ng of RNA, using SuperScript™ III First-Strand Synthesis System (Thermo Scientific, 18080051). Quantitative real-time PCR (qPCR) was performed using the PerfeCTa SYBR green FastMix (Quanta Biosciences) and gene-specific primers for Inpp5f and Gapdh, on the ViiA-7 system (Thermo Fisher Scientific). For RT-ddPCR, RNA was isolated from DRG neurons, using RNeasy Microisolation Kit (QIAGEN). Fluorimetry with Ribogreen (Life Technologies) was used for RNA quantification; 20 ng of RNA was used for reverse transcription (RT) with SensiFAST cDNA synthesis kit (Bioline) according to the manufacturer's protocol. ddPCR was performed using custom *Ncl* mRNA-specific primer sets (IDT; forward primer: 5′CGGAAGAGGCGGATTTGG3′; reverse primer: 5′GGAAAGAATGGGATGGAAGGA3′) and detected with Evagreen using a QX200TM droplet reader (Bio-Rad).

Axon outgrowth analysis

For outgrowth analysis, nucleolin $GAR^{+/-}$ and wild-type mice were crossed with Thy1-YFP mice (Feng *et al*, 2000). DRG neurons from adult mice were plated on 35-mm glass-bottom dishes (MatTek) coated with poly-L-lysine and laminin. After seeding, neurons were imaged every hour for 48 h using Fluoview (FV10), a fully automated confocal laser-scanning microscope with a built-in CO2

incubator, at a 60× magnification. 3 × 3 neighboring sites were montaged and analyzed using ImageJ, as previously described (Perry *et al*, 2016).

For outgrowth analysis in GAR-overexpressing neurons, cultured DRG neurons from adult C57/Bl6 mice were infected with AAV-PHP.s encoding HA-Dendra2-GAR(WT) or HA-Dendra2-GAR(N) on seeding. At 8–10 days *in vitro* cells were replated onto new coverslips for an additional 24 h, fixed, and stained for NFH and HA. Images were captured at 10× magnification on ImageXpress Micro (Molecular Devices), and infected cells were analyzed using the Metamorph software (Molecular Devices). The total outgrowth parameter was defined as the sum of all process lengths.

Quantification and statistical analysis

Data shown represent mean ± SEM, unless otherwise noted. N represents number of independent biological repeats, unless otherwise mentioned. Statistical analyses and graphs were generated using GraphPad Prism 8 software. Pairwise analyses were conducted by paired two-tailed *t*-test (Figs 1F, 2E, 3E and 5C) or unpaired two-tailed *t*-test with homoscedasticity (Figs 6B, D and F, and 7E and F), depending on experimental design. Mann–Whitney non-parametric test was used for Fig 4B and Appendix Fig S4B and D since the data did not fit a Gaussian distribution. Groupwise analyses were conducted by one-way ANOVA for one-factor analyses assuming equal variances (Appendix Fig S3B and E, Figs 3C and H, and 8C and D) or two-way ANOVA where > 1 factor was analyzed (Figs 1B, 2B and G, 4D, and 9B and D Appendix Figs S1C and S4F and H). Shapiro–Wilk test was used to test for data normality. Linear binomial test was used in Appendix Fig S5C. Statistically significant *P*-values are shown as $*P < 0.05$, $**P < 0.01$, $***P < 0.001$ and $****P < 0.0001$.

Data availability

- Gene expression analysis (RNA-seq) data generated from this paper have been deposited in NCBI's Gene Expression Omnibus (GEO) and are accessible through GEO series accession number: GSE142576 (https://www.ncbi.nlm.nih.gov/geo/query/acc.cgi?acc=GSE142576).
- Scripts used in the RNA sequencing analyses are available at https://github.com/icnn/RNAseq-PIPELINE.git.
- The mass spectrometry proteomic data have been deposited to the ProteomeXchange Consortium via the PRIDE (Perez-Riverol *et al*, 2019) partner repository with the dataset identifier PXD020804 (http://proteomecentral.proteomexchange.org/cgi/GetDataset?ID=PXD020804).

Expanded View for this article is available online.

Acknowledgements
We sincerely thank Andres Ramos (University College London) for valuable insights, Vladimir Kiss, and Reinat Nevo for assistance with microscopy; Yael Fridmann-Sirkis for assistance with surface plasmon resonance; and Yarden Tzur, Rotem Perry, and Avraham Yaron for helpful discussions. We gratefully acknowledge funding from the Israel Science Foundation (ISF 1337/18 to MF), the Dr. Miriam and Sheldon G. Adelson Medical Research Foundation (to GC, ALB, JLT & MF), the National Institutes of Health (K01NS105879 to TPS, R01NS117821 and R01NS089633 to JLT, P41GM103481, and 1S10OD016229 to ALB), the South Carolina Spinal Cord Injury Research Fund (2019 PD-02 to PKS), and the Czech Science Foundation (EXPRO 19-26854X to PJ).

Author contributions
ED-M, IK, and MF designed the study; ED-M, IK, OA, IR, JK, SA, EEZ, PD-M, AD-P, D-AS, NO, and DG planned and performed experiments, simulations, and data analyses; TPS, CNB and PKS conducted FISH analyses; SB-D performed bioinformatics analyses, JAO-P carried out mass spectrometry analyses; RK performed RNA-seq analyses; RH-K generated the CRISPR engineered mice; GC, ALB, PJ, JLT, and MF supervised research; ED-M, IK, and MF wrote the manuscript draft. All authors revised the manuscript and approved the final version.

Conflict of interest
The authors declare that they have no conflict of interest.

References

Abraham MJ, Murtola T, Schulz R, Páll S, Smith JC, Hess B, Lindahl E (2015) GROMACS: High performance molecular simulations through multi-level parallelism from laptops to supercomputers. *SoftwareX* 1–2: 19 – 25

Albus CA, Rishal I, Fainzilber M (2013) Cell length sensing for neuronal growth control. *Trends Cell Biol* 23: 305 – 310

Allolio C, Magarkar A, Jurkiewicz P, Baxová K, Javanainen M, Mason PE, Šachl R, Cebecauer M, Hof M, Horinek D *et al* (2018) Arginine-rich cell-penetrating peptides induce membrane multilamellarity and subsequently enter via formation of a fusion pore. *Proc Natl Acad Sci USA* 115: 11923 – 11928

Bates PJ, Reyes-Reyes EM, Malik MT, Murphy EM, O'Toole MG, Trent JO (2017) G-quadruplex oligonucleotide AS1411 as a cancer-targeting agent: uses and mechanisms. *Biochim Biophys Acta* 1861: 1414 – 1428

Baumann S, Komissarov A, Gili M, Ruprecht V, Wieser S, Maurer SP (2020) A reconstituted mammalian APC-kinesin complex selectively transports defined packages of axonal mRNAs. *Sci Adv* 6: eaaz1588

Berger CM, Gaume X, Bouvet P (2015) The roles of nucleolin subcellular localization in cancer. *Biochimie* 113: 78 – 85

Chan KY, Jang MJ, Yoo BB, Greenbaum A, Ravi N, Wu W-L, Sánchez-Guardado L, Lois C, Mazmanian SK, Deverman BE *et al* (2017) Engineered AAVs for efficient noninvasive gene delivery to the central and peripheral nervous systems. *Nat Neurosci* 20: 1172 – 1179

Chong PA, Vernon RM, Forman-Kay JD (2018) RGG/RG Motif regions in RNA binding and phase separation. *J Mol Biol* 430: 4650 – 4665

Cioni J-M, Lin JQ, Holtermann AV, Koppers M, Jakobs MAH, Azizi A, Turner-Bridger B, Shigeoka T, Franze K, Harris WA *et al* (2019) Late endosomes act as mRNA translation platforms and sustain mitochondria in axons. *Cell* 176: 56 – 72.e15

Clauser KR, Baker P, Burlingame AL (1999) Role of accurate mass measurement (+/- 10 ppm) in protein identification strategies employing MS or MS/MS and database searching. *Anal Chem* 71: 2871 – 2882

Creancier L, Prats H, Zanibellato C, Amalric F, Bugler B (1993) Determination of the functional domains involved in nucleolar targeting of nucleolin. *Mol Biol Cell* 4: 1239 – 1250

Darden T, York D, Pedersen L (1993) Particle Mesh Ewald - an N.Log(N) method for Ewald sums in large systems. *J Chem Phys* 98: 10089 – 10092

Darnell JC, Jensen KB, Jin P, Brown V, Warren ST, Darnell RB (2001) Fragile X mental retardation protein targets G quartet mRNAs important for neuronal function. *Cell* 107: 489 – 499

Farin K, Schokoroy S, Haklai R, Cohen-Or I, Elad-Sfadia G, Reyes-Reyes ME, Bates PJ, Cox AD, Kloog Y, Pinkas-Kramarski R (2011) Oncogenic synergism between ErbB1, nucleolin, and mutant Ras. *Cancer Res* 71: 2140 – 2151

Feng G, Mellor RH, Bernstein M, Keller-Peck C, Nguyen QT, Wallace M, Nerbonne JM, Lichtman JW, Sanes JR (2000) Imaging neuronal subsets in transgenic mice expressing multiple spectral variants of GFP. *Neuron* 28: 41 – 51

Gershoni-Emek N, Altman T, Ionescu A, Costa CJ, Gradus-Pery T, Willis DE, Perlson E (2018) Localization of RNAi machinery to axonal branch points and growth cones is facilitated by mitochondria and is disrupted in ALS. *Front Mol Neurosci* 11: 311

Gilles M-E, Maione F, Cossutta M, Carpentier G, Caruana L, Di Maria S, Houppe C, Destouches D, Shchors K, Prochasson C *et al* (2016) Nucleolin targeting impairs the progression of pancreatic cancer and promotes the normalization of tumor vasculature. *Cancer Res* 76: 7181 – 7193

Goering R, Hudish LI, Guzman BB, Raj N, Bassell GJ, Russ HA, Dominguez D, Taliaferro JM (2020) FMRP promotes RNA localization to neuronal projections through interactions between its RGG domain and G-quadruplex RNA sequences. *Elife* 9: e52621

Guan S, Price JC, Prusiner SB, Ghaemmaghami S, Burlingame AL (2011) A data processing pipeline for mammalian proteome dynamics studies using stable isotope metabolic labeling. *Mol Cell Proteomics* 10:M111.010728.

Guccione E, Richard S (2019) The regulation, functions and clinical relevance of arginine methylation. *Nat Rev Mol Cell Biol* 20: 642 – 657

Herce HD, Garcia AE, Cardoso MC (2014) Fundamental molecular mechanism for the cellular uptake of guanidinium-rich molecules. *J Am Chem Soc* 136: 17459 – 17467

Hess B, Bekker H, Berendsen HJC, Fraaije JGEM (1997) LINCS: a linear constraint solver for molecular simulations. *J Comput Chem* 18: 1463 – 1472

Hirokawa N, Noda Y, Tanaka Y, Niwa S (2009) Kinesin superfamily motor proteins and intracellular transport. *Nat Rev Mol Cell Biol* 10: 682 – 696

Hockney RW, Goel SP, Eastwood JW (1974) Quiet high-resolution computer models of a plasma. *J Comput Phys* 14: 148 – 158

Hofweber M, Hutten S, Bourgeois B, Spreitzer E, Niedner-Boblenz A, Schifferer M, Ruepp M-D, Simons M, Niessing D, Madl T *et al* (2018) Phase separation of FUS is suppressed by its nuclear import receptor and arginine methylation. *Cell* 173: 706 – 719.e13

Hsu F, Hu F, Mao Y (2015) Spatiotemporal control of phosphatidylinositol 4-phosphate by Sac2 regulates endocytic recycling. *J Cell Biol* 209: 97 – 110

Humphrey W, Dalke A, Schulten K (1996) VMD: visual molecular dynamics. *J Mol Graph Model* 14: 33 – 38

Jorgensen WL, Chandrasekhar J, Madura JD, Impey RW, Klein ML (1983) Comparison of simple potential functions for simulating liquid water. *J Chem Phys* 79: 926 – 935

Kapeli K, Martinez FJ, Yeo GW (2017) Genetic mutations in RNA-binding proteins and their roles in ALS. *Hum Genet* 136: 1193 – 1214

Klauda JB, Venable RM, Freites JA, O'Connor JW, Tobias DJ, Mondragon-Ramirez C, Vorobyov I, MacKerell AD, Pastor RW (2010) Update of the CHARMM all-atom additive force field for lipids: validation on six lipid types. *J Phys Chem B* 114: 7830 – 7843

Lamaziere A, Burlina F, Wolf C, Chassaing G, Trugnan G, Ayala-Sanmartin J (2007) Non-metabolic membrane tubulation and permeability induced by bioactive peptides. *PLoS One* 2: e201

Lee J, Sayegh J, Daniel J, Clarke S, Bedford MT (2005) PRMT8, a new membrane-bound tissue-specific member of the protein arginine methyltransferase family. *J Biol Chem* 280: 32890 – 32896

Leontyev I, Stuchebrukhov A (2011) Accounting for electronic polarization in non-polarizable force fields. *Phys Chem Chem Phys* 13: 2613 – 2626

Liao YC, Fernandopulle MS, Wang G, Choi H, Hao L, Drerup CM, Patel R, Qamar S, Nixon-Abell J, Shen Y *et al* (2019) RNA granules hitchhike on lysosomes for long-distance transport, using annexin A11 as a molecular tether. *Cell* 179: 147 – 164 e120

Mahn M, Gibor L, Patil P, Cohen-Kashi Malina K, Oring S, Printz Y, Levy R, Lampl I, Yizhar O (2018) High-efficiency optogenetic silencing with soma-targeted anion-conducting channelrhodopsins. *Nat Commun* 9: 4125

Marvaldi L, Panayotis N, Alber S, Dagan SY, Okladnikov N, Koppel I, Di Pizio A, Song DA, Tzur Y, Terenzio M *et al* (2020) Importin alpha3 regulates chronic pain pathways in peripheral sensory neurons. *Science* 369: 842 – 846

Masuzawa T, Oyoshi T (2020) Roles of the RGG domain and RNA recognition motif of nucleolin in G-quadruplex stabilization. *ACS Omega* 5: 5202 – 5208

Mishra A, Lai GH, Schmidt NW, Sun VZ, Rodriguez AR, Tong R, Tang L, Cheng J, Deming TJ, Kamei DT *et al* (2011) Translocation of HIV TAT peptide and analogues induced by multiplexed membrane and cytoskeletal interactions. *Proc Natl Acad Sci USA* 108: 16883 – 16888

Miyamoto S, Kollman PA (1992) Settle - an analytical version of the shake and rattle algorithm for rigid water models. *J Comput Chem* 13: 952 – 962

Nott T, Petsalaki E, Farber P, Jervis D, Fussner E, Plochowietz A, Craggs TD, Bazett-Jones D, Pawson T, Forman-Kay J *et al* (2015) Phase transition of a disordered nuage protein generates environmentally responsive membraneless organelles. *Mol Cell* 57: 936 – 947

Okuwaki M, Saotome-Nakamura A, Yoshimura M, Saito S, Hirawake-Mogi H, Sekiya T, Nagata K (2020) RNA-recognition motifs and glycine and arginine-rich region cooperatively regulate the nucleolar localization of nucleolin. *J Biochem* 169: 87 – 100

Pae J, Saalik P, Liivamagi L, Lubenets D, Arukuusk P, Langel U, Pooga M (2014) Translocation of cell-penetrating peptides across the plasma membrane is controlled by cholesterol and microenvironment created by membranous proteins. *J Control Release* 192: 103 – 113

Park SW, Jun YW, Choi HE, Lee JA, Jang DJ (2019) Deciphering the molecular mechanisms underlying the plasma membrane targeting of PRMT8. *BMB Rep* 52: 601 – 606

Pellar GJ, DiMario PJ (2003) Deletion and site-specific mutagenesis of nucleolin's carboxy GAR domain. *Chromosoma* 111: 461 – 469

Perez-Riverol Y, Csordas A, Bai J, Bernal-Llinares M, Hewapathirana S, Kundu DJ, Inuganti A, Griss J, Mayer G, Eisenacher M *et al* (2019) The PRIDE database and related tools and resources in 2019: improving support for quantification data. *Nucleic Acids Res* 47: D442 – D450

Perry R-T, Rishal I, Doron-Mandel E, Kalinski AL, Medzihradszky KF, Terenzio M, Alber S, Koley S, Lin A, Rozenbaum M *et al* (2016) Nucleolin-mediated RNA localization regulates neuron growth and cycling cell size. *Cell Rep* 16: 1664 – 1676

Plaisier SB, Taschereau R, Wong JA, Graeber TG (2010) Rank-rank hypergeometric overlap: identification of statistically significant overlap between gene-expression signatures. *Nucleic Acids Res* 38: e169

Ramos A, Hollingworth D, Pastore A (2003) G-quartet-dependent recognition between the FMRP RGG box and RNA. *RNA* 9: 1198 – 1207

Ran FA, Hsu PD, Wright J, Agarwala V, Scott DA, Zhang F (2013) Genome engineering using the CRISPR-Cas9 system. *Nat Protoc* 8: 2281 – 2308

Rishal I, Fainzilber M (2019) Cell size sensing - a one-dimensional solution for a three-dimensional problem? *BMC Biol* 17: 36

Rishal I, Kam N, Perry RB, Shinder V, Fisher EM, Schiavo G, Fainzilber M (2012) A motor-driven mechanism for cell-length sensing. *Cell Rep* 1: 608 – 616

Romano S, Fonseca N, Simoes S, Goncalves J, Moreira JN (2019) Nucleolin-based targeting strategies for cancer therapy: from targeted drug delivery to cytotoxic ligands. *Drug Discov Today* 24: 1985 – 2001

Saha A, Duchambon P, Masson V, Loew D, Bombard S, Teulade-Fichou MP (2020) Nucleolin discriminates drastically between long-loop and short-loop quadruplexes. *Biochemistry* 59: 1261 – 1272

Sahoo PK, Kar AN, Samra N, Terenzio M, Patel P, Lee SJ, Miller S, Thames E, Jones B, Kawaguchi R *et al* (2020) A Ca(2+)-dependent switch activates axonal casein kinase 2alpha translation and drives G3BP1 granule disassembly for axon regeneration. *Curr Biol* 30: 4882 – 4895 e4886

Sahoo PK, Lee SJ, Jaiswal PB, Alber S, Kar AN, Miller-Randolph S, Taylor EE, Smith T, Singh B, Ho T-Y *et al* (2018) Axonal G3BP1 stress granule protein limits axonal mRNA translation and nerve regeneration. *Nat Commun* 9: 3358

Schmidt-Zachmann MS, Nigg EA (1993) Protein localization to the nucleolus: a search for targeting domains in nucleolin. *J Cell Sci* 105(Pt 3): 799 – 806

Storck S, Thiry M, Bouvet P (2009) Conditional knockout of nucleolin in DT40 cells reveals the functional redundancy of its RNA-binding domains. *Biol Cell* 101: 153 – 167

Sun D, Forsman J, Lund M, Woodward CE (2014) Effect of arginine-rich cell penetrating peptides on membrane pore formation and life-times: a molecular simulation study. *Phys Chem Chem Phys* 16: 20785 – 20795

Takeuchi T, Futaki S (2016) Current understanding of direct translocation of arginine-rich cell-penetrating peptides and its internalization mechanisms. *Chem Pharm Bull* 64: 1431 – 1437

Tanikawa C, Ueda K, Suzuki A, Iida A, Nakamura R, Atsuta N, Tohnai G, Sobue G, Saichi N, Momozawa Y *et al* (2018) Citrullination of RGG Motifs in FET proteins by PAD4 regulates protein aggregation and ALS susceptibility. *Cell Rep* 22: 1473 – 1483

Teo G, Liu G, Zhang J, Nesvizhskii AI, Gingras AC, Choi H (2014) SAINTexpress: improvements and additional features in significance analysis of INTeractome software. *J Proteomics* 100: 37 – 43

Terenzio M, Koley S, Samra N, Rishal I, Zhao Q, Sahoo PK, Urisman A, Marvaldi L, Oses-Prieto JA, Forester C *et al* (2018) Locally translated mTOR controls axonal local translation in nerve injury. *Science* 359: 1416 – 1421

Thandapani P, O'Connor TR, Bailey TL, Richard S (2013) Defining the RGG/RG motif. *Mol Cell* 50: 613 – 623

Tsang B, Arsenault J, Vernon RM, Lin H, Sonenberg N, Wang LY, Bah A, Forman-Kay JD (2019) Phosphoregulated FMRP phase separation models activity-dependent translation through bidirectional control of mRNA granule formation. *Proc Natl Acad Sci USA* 116: 4218 – 4227

Twiss JL, Smith DS, Chang B, Shooter EM (2000) Translational control of ribosomal protein L4 mRNA is required for rapid neurite regeneration. *Neurobiol Dis* 7: 416 – 428

Ugrinova I, Monier K, Ivaldi C, Thiry M, Storck S, Mongelard F, Bouvet P (2007) Inactivation of nucleolin leads to nucleolar disruption, cell cycle arrest and defects in centrosome duplication. *BMC Mol Biol* 8: 66

Ugrinova I, Petrova M, Chalabi-Dchar M, Bouvet P (2018) Multifaceted nucleolin protein and its molecular partners in oncogenesis. *Adv Protein Chem Struct Biol* 111: 133 – 164

Vasilyev N, Polonskaia A, Darnell JC, Darnell RB, Patel DJ, Serganov A (2015) Crystal structure reveals specific recognition of a G-quadruplex RNA by a beta-turn in the RGG motif of FMRP. *Proc Natl Acad Sci USA* 112: E5391 – 5400

Vazdar M, Heyda J, Mason PE, Tesei G, Allolio C, Lund M, Jungwirth P (2018) Arginine "Magic": guanidinium like-charge ion pairing from aqueous salts to cell penetrating peptides. *Acc Chem Res* 51: 1455 – 1464

Willis DE, Twiss JL (2011) Profiling axonal mRNA transport. *Methods Mol Biol* 714: 335 – 352

Wu EL, Cheng X, Jo S, Rui H, Song KC, Davila-Contreras EM, Qi YF, Lee JM, Monje-Galvan V, Venable RM *et al* (2014) CHARMM-GUI membrane builder toward realistic biological membrane simulations. *J Comput Chem* 35: 1997 – 2004

Wu H, Zhou J, Zhu T, Cohen I, Dictenberg J (2020) A kinesin adapter directly mediates dendritic mRNA localization during neural development in mice. *J Biol Chem* 295: 6605 – 6628

Yagi R, Miyazaki T, Oyoshi T (2018) G-quadruplex binding ability of TLS/FUS depends on the beta-spiral structure of the RGG domain. *Nucleic Acids Res* 46: 5894 – 5901

Zhu W, Trivedi CM, Zhou D, Yuan L, Lu MM, Epstein JA (2009) Inpp5f is a polyphosphoinositide phosphatase that regulates cardiac hypertrophic responsiveness. *Circ Res* 105: 1240 – 1247

Zou Y, Stagi M, Wang X, Yigitkanli K, Siegel CS, Nakatsu F, Cafferty WB, Strittmatter SM (2015) Gene-silencing screen for mammalian axon regeneration identifies Inpp5f (Sac2) as an endogenous suppressor of repair after spinal cord injury. *J Neurosci* 35: 10429 – 10439